frontiers in Materials

TYPE Review
PUBLISHED 21 October 2026
DOI 10.3389/fmats.2026.1954859

Check for updates

OPEN ACCESS

EDITED BY
Mattia Franceschi,
Spanish National Research Council (CSIC), Spain

REVIEWED BY
Jessy Michla J. R.,
Kalasalingam University, India
Harsha B P,
PES Institute of Technology and Management, India

*CORRESPONDENCE
Sudipta Mohapatra,
dipusudipta57@gmail.com

RECEIVED 31 July 2026
REVISED 14 September 2026
ACCEPTED 29 September 2026
PUBLISHED 21 October 2026

CITATION
Mohapatra S, Pradhan R, Mahapatra BN and Swain PK (2026) A comprehensive review on development of texture in automotive-grade medium manganese steel.
Front. Mater. 13:1954859.
doi: 10.3389/fmats.2026.1954859

COPYRIGHT
© 2026 Mohapatra, Pradhan, Mahapatra and Swain. This is an open-access article distributed under the terms of the Creative Commons Attribution License (CC BY). The use, distribution or reproduction in other forums is permitted, provided the original author(s) and the copyright owner(s) are credited and that the original publication in this journal is cited, in accordance with accepted academic practice. No use, distribution or reproduction is permitted which does not comply with these terms.

A comprehensive review on development of texture in automotive-grade medium manganese steel

Sudipta Mohapatra[1]*, Rururaja Pradhan[1], Bishnu Narayan Mahapatra[1] and Prasant Kumar Swain[2]

[1]School of Mechanical Sciences, Odisha University of Technology and Research, Bhubaneswar, India, [2]Department of Mechanical Engineering, National Institute of Advanced Manufacturing Technology, Ranchi, India

Medium manganese steels (MMnSs, 3–12 wt% Mn) are pivotal for third-generation automotive applications due to their strong strength-ductility synergy from complex phase transformations and texture evolution. This review discusses the latest findings in texture development across ferritic, austenitic, and duplex MMnSs, focusing on the influence of alloying elements, stacking fault energy (SFE), and austenite reversion during processing. Studies show that γ-fiber strengthening, cube orientation, and twinning-induced reorientation affect mechanical anisotropy and crashworthiness. Key elements like Mn, Ni, and C stabilize austenite and foster γ-fiber textures, while Al and Si decrease SFE to enhance twinning and ferritic cube components. Despite significant progress, challenges in predicting quantitative prediction of texture evolution under industrial processing conditions, the stability of reverted austenite during cyclic loading, and the integration of TRIP/TWIP mechanisms into predictive models persist. Research gaps include the need for advanced *in-situ* characterization, multiscale simulations linking chemistry to texture, and long-term corrosion-mechanical coupling studies. By identifying these challenges, this review provides a roadmap for alloy design and processing strategies aimed at optimizing the strength–ductility balance of MMnSs for next-generation automotive steels.

KEYWORDS
austenite, intercritical annealing, medium-manganese steel, texture evolution, TRIP effect

1 Introduction

1.1 Background

The automotive industry is actively working to enhance fuel efficiency and component performance while simultaneously reducing CO_2 emissions and vehicle weight (Raabe et al., 2009; Ma et al., 2020; Suh and Kim, 2017; Li et al., 2018a; Yadav et al., 2023). A significant development in this effort is the use of advanced high-strength steels (AHSSs), which are recognized for their lightweight characteristics (Figure 1). AHSS has exceptional ductility, toughness, and fatigue resistance, making it suitable for various vital components of vehicles, including undercarriages, vehicle bodies, frames, bumpers, and doors (De Cooman et al., 2012). AHSS is categorized into three generations (Soleimani et al., 2020; Chen et al., 2017; Lee and Han, 2015; Hu et al., 2019;

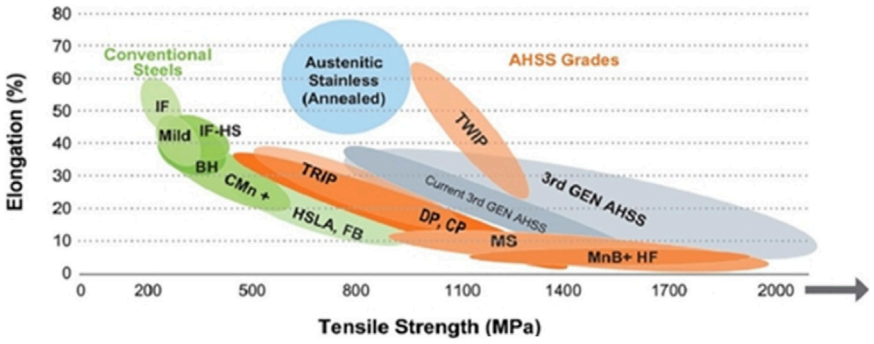

FIGURE 1
Comparison of the tensile strength (TS) and total elongation (TE) of different classes of conventional and advanced high-strength steels (AHSSs). Adopted with permission (Jacob et al., 2019).

Zhang et al., 2018): (1) The first-generation AHSS includes low-Mn martensitic steels, transformation-induced plasticity (TRIP) steels, dual-phase (DP) steels, and complex-phase (CP) steels, which are designed to improve vehicle performance and safety (Zou et al., 2017; Li ZC. et al., 2017; Zhou et al., 2018). (2) The second generation introduces twinning-induced plasticity steels, nano-twinning-induced plasticity (TWIP) steels, and duplex and triplex steels, which address issues of lower ductility found in first-generation materials (Dalai et al., 2026). These are applied in structural components, barrier systems, and various safety features in vehicles (Sun et al., 2022; Mohapatra et al., 2026a). (3) Third-generation AHSS, which includes medium-manganese steel (MMnS) (Cai et al., 2016; Mishra et al., 2017; Dutta et al., 2019; Mohapatra et al., 2023a), quenching and partitioning (Q&P) steel (Zinsaz-borujerdi et al., 2018; Dai et al., 2018; Seo et al., 2016; Hu et al., 2023), and carbide-free bainite (CFB) steel (Bhadeshia, 2005; Soliman and Palkowski, 2014), has gained traction due to its ability to further lower CO_2 emissions and enhance fuel efficiency. MMnSs are particularly notable for their superior strength-to-elongation ratios and are cost-effective alternatives to high-manganese TWIP steels. TWIP, TRIP, ferritic-bainitic (FB), and martensitic (MS) steels also significantly contribute to structural integrity and safety standards in automotive manufacturing.

1.2 Automotive-grade medium manganese steel (MMnS)

MMnS with 3–12 wt% Mn is proposed as a viable option for third-generation AHSS, aiming to achieve an optimal balance of strength and ductility while minimizing production costs and enhancing crash resistance (Lee and Han, 2015; Hu et al., 2017; Dalai et al., 2023; Mohapatra, 2023; Mohapatra et al., 2026b; Wang et al., 2019). The demand for lightweight Fe-Mn-Al-C MMnS has surged due to their favorable tensile properties and reduced density, which are advantageous for automotive applications (Mohapatra et al., 2022; Yu and Deng, 2025). The density regulation of these steels is influenced by aluminum (Al) content; although higher Al levels lower density, they also lead to the formation of non-metallic Al inclusions such as Al_2O_3 and Fe_3Al intermetallic compounds, which can adversely affect the desired strength-ductility combination in these advanced materials. Consequently, maintaining a limited Al concentration in AHSS is crucial to prevent the development of brittle intermetallic precipitates. These steels can be classified into three categories: ferritic, austenitic, and duplex steels, which comprise both ferrite and austenite phases (Hui et al., 2017; Shao et al., 2017). The tensile properties of single-phase ferritic steel can be enhanced through the generation of the austenite phase during various heat treatments and the transformation of unstable austenite into martensite during tensile stress application, leveraging the TRIP effect (Zou et al., 2017; Luo et al., 2017; Pütz et al., 2021). The latest generation of AHSS utilizes TRIP to optimize the interplay between strength and ductility, significantly enhancing work hardening behavior and this key relationship. Furthermore, the introduction of alloying elements such as nickel (Ni) can improve the strength-ductility relationship via mechanisms of precipitation and solid solution strengthening. Studies have shown that integrating TRIP mechanisms with B_2(NiAl) precipitation can result in exceptional tensile properties in nickel-enriched MMnS (Lee et al., 2013; Peng et al., 2018; Han et al., 2011; Kumar et al., 2023; Cheng et al., 2019; Cai et al., 2014).

Common processing techniques used in MMnS include intercritical annealing (IA), quenching and partitioning (Q&P), and quenching and tempering (Q&T) (Li et al., 2018a; Mohapatra et al., 2023b; Li et al., 2016). Different initial microstructures prior to IA can influence the morphology of RA. Austenite reversion and precipitation are influenced by hot and cold deformation prior to heat treatment. Nevertheless, the formation of sizable precipitates requires further annealing treatment. Through adequate element partitioning, IA can generate a suitable amount of austenite to facilitate stabilization. A novel method of moderate temperature modulation allows for the continuous reversion of austenite while also promoting nanoprecipitation. The mechanical performance of medium Mn steels is contingent upon the microstructure optimization of retained austenite (RA) and nano-sized particles. The design of a new steel with a suitable IA processing window, along with enhanced RA stability, is of utmost importance to achieve the optimal TRIP effect (Sahoo et al., 2021; Poojari et al., 2024; Han et al., 2017). The presence of RA stabilizes the TRIP and

TABLE 1 Automotive relevance of key texture components in MMnSs, highlighting their influence on formability, anisotropy, and strain-hardening behavior.

Texture component	Automotive impact
γ-fiber ({111}//ND)	High plastic strain ratio, excellent deep drawability, improved ductility
Cube ({001} < 100>)	Balanced isotropy, reduced springback, dimensional accuracy
Goss ({110} < 001>)	Influences recrystallization, can reduce anisotropy if controlled
Brass ({110} < 112>)	Associated with deformation twinning, enhances strain hardening

TWIP mechanisms, leading to enhanced strain hardening. The uniform precipitation of nano-sized particles is closely associated with segregation, while the morphology and mechanical stability of austenite can be regulated by element diffusion. Metastable austenite with varying micro-mechanical stability is the result of cold deformation prior to austenite reversion treatment, which is attributed to the non-uniform distribution of element content, grain size, and dislocation density. The interface migration rate of the kinematic growth mode is regulated by Mn diffusion across the austenite/ferrite phase boundaries. Mn segregation favorably to precipitates can significantly influence TRIP effects by reducing the concentration in solid solution and the stacking fault energy (SFE) of austenite (Li ZC. et al., 2017; Hui et al., 2017; Shao et al., 2017; Li et al., 2018b; Steineder et al., 2017).

1.3 Importance of texture in automotive applications

Texture plays a crucial role in automotive applications, particularly in the mechanical anisotropy, formability, and crashworthiness of advanced steels utilized in vehicle structures (Xie and Nakamachi, 2002; Raabe, 1997; Mohapatra et al., 2024a). Its importance can be dissected into several key aspects: Automotive body panels necessitate superior deep-drawing performance. A strong γ-fiber ({111}//ND) texture enhances the plastic strain ratio (r-value), which in turn minimizes thinning and heightens sheet formability. This leads to smoother stamping processes and reduces manufacturing defects. Texture is instrumental in dictating the distribution of slip systems and twinning mechanisms within the steel. An optimized combination of γ-fiber and cube textures enables the achievement of the TRIP and TWIP effects (Mandal, 2016). This balance is critical for developing lightweight yet crash-resistant automotive designs. The influence of texture extends to the strain hardening behavior and uniform elongation of the material. Steels with refined γ-fiber textures demonstrate higher strain hardening rates, allowing them to absorb more energy in the event of an impact, thus significantly enhancing passenger safety during crashes (Mohapatra et al., 2026b; Mohapatra et al., 2023c). Poorly controlled textures can lead to mechanical anisotropy, which results in uneven deformation in vehicle panels. By managing texture evolution effectively, manufacturers can ensure isotropy, reduce spring back and enhance dimensional accuracy in automotive components. Texture also affects the distribution of grain boundary characters, specifically CSL boundaries. Optimized texture variations increase the prevalence of these special boundaries, thereby improving resistance to intergranular corrosion and fatigue cracking—vital for the long-term durability of vehicles. The details of different texture components and their importance are presented in Table 1.

1.4 Scope of this review

This paper provides a comprehensive synthesis of texture development in MMnS, structured as follows:

- Section 2: Evolution of Texture
- Section 3: Microstructural classes and texture mechanisms
- Section 4: Role of alloying elements on texture
- Section 5: Texture evolution associated with mechanical properties
- Section 6: Overview of this work
- Section 7: Research gaps, challenges, and perspectives
- Section 8: Conclusions

This review work comprehensively synthesizes texture development in automotive-grade-MMnSs. It systematically compares ferritic, austenitic, and duplex MMnSs classes, linking texture components to mechanisms (TRIP/TWIP) and mechanical implications. The manuscript highlights the influence of alloying elements (Mn, Ni, C, Al, and Si) on SFE and texture evolution. It connects microstructural observations to automotive applications, discussing anisotropy, establishing texture evolution as the central design parameter for optimizing strength-ductility balance in next-generation automotive steels.

2 Evolution of texture

Texture-induced anisotropy significantly influences the deep drawability and formability properties, YS, and elastic modulus of BCC steels (Xie and Nakamachi, 2002; Raabe, 1997; Mohapatra et al., 2024a). The properties are enhanced by the ND or γ-fibers present in the ferrite phase, whereas cleavage fractures are propagated by the (001) planes in BCC materials (Ghosh et al., 2014). Delamination behavior is adversely affected by the cube fiber texture, specifically the (001) ⟨110⟩ orientation (Ghosh et al., 2016). Thus, it is more advantageous to deduce from previous research that the formation of cube fibers should be limited to achieve superior tensile properties. The YS is reportedly enhanced when the transformation texture contains a greater proportion of fibers in the (113) ⟨110⟩ orientation, which is a substantial constituent of RD//⟨110⟩ fiber (Hutchinson et al., 2005). Like the BCC phase, the tensile properties are significantly influenced by

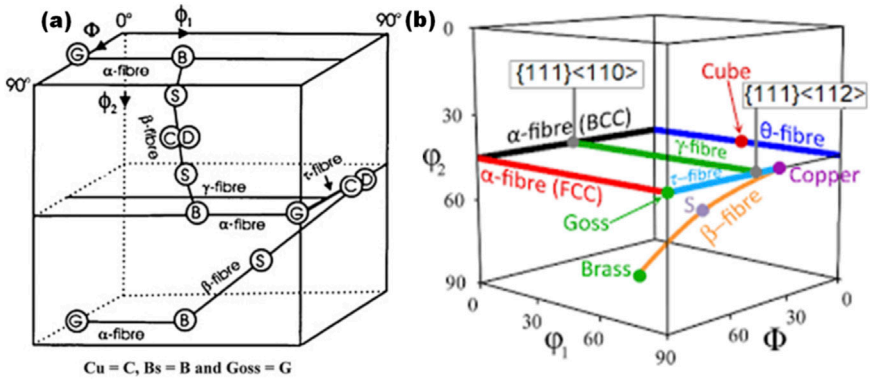

FIGURE 2
(a) Three-dimensional Euler's space showing important components and **(b)** orientations of the standard FCC texture at the ϕ_2 = 45° section. Reproduced with permission (Suwas et al., 2014).

the textural components of the FCC phase. Barbier et al. explained that superior tensile properties can be achieved by incorporating brass component texture intensities into high-manganese TWIP steel during deformation (Barbier et al., 2009). However, MMnS exhibits distinct characteristics. The following are some of the studies conducted on the evolution of texture and its correlation with the mechanical behavior of MMnS.

2.1 Rolling texture in FCC-austenite phase

The SFE of the material influences the evolution of textural components of the FCC-austenite phase (Suwas et al., 2014; Capek et al., 2018). Materials with lower SFE exhibit the formation of brass-type (110) < 1 $\bar{1}$ 2> and Goss-type (011) ⟨100⟩ components, while materials with higher SFE develop Cu-type (112) ⟨111⟩ components (Suwas et al., 2014). The α, τ, and β phases are the primary sources of fibers for the FCC-austenite phase. The primary texture fiber is composed of brass, Cu, and cube components, specifically the α-fiber (⟨011⟩//ND) (Raabe, 1997).The α-fiber of the FCC phase shifts from the Goss component (110) ⟨001⟩ to the brass component (110) < 1 $\bar{1}$ 2> (Pradhan et al., 2024). The τ-fiber of the FCC phase, oriented along the ⟨110⟩ direction with respect to the transverse direction (TD), extends from the (001) ⟨110⟩ plane through the Cu position to the Goss components located at the (110) ⟨001⟩ plane Figure 2a (Raabe, 1997; Suwas et al., 2014; Capek et al., 2018). The β-fiber is an asymmetrical fiber that spans from the Cu location (112) ⟨111⟩ to the α-fiber at the brass position (110) < 1 $\bar{1}$ 2> through the S orientation (123) ⟨634⟩ (Raabe, 1997; Suwas et al., 2014). Figure 2b illustrates the ideal orientations for FCC-austenite in Euler's space at ϕ2 = 45°.

2.2 Rolling texture in BCC-ferrite phase

The BCC-ferrite phase of BCC metals is characterized by the development of textural elements, such as α, γ, η, and ε fibers, which are associated with a specific fiber orientation in Euler's space (Xie and Nakamachi, 2002). The terms "RD" and "ND" fibers correspond to α- and γ-fibers, respectively. Figure 3 shows the optimal orientations for BCC-ferrite in Euler's space, specifically at

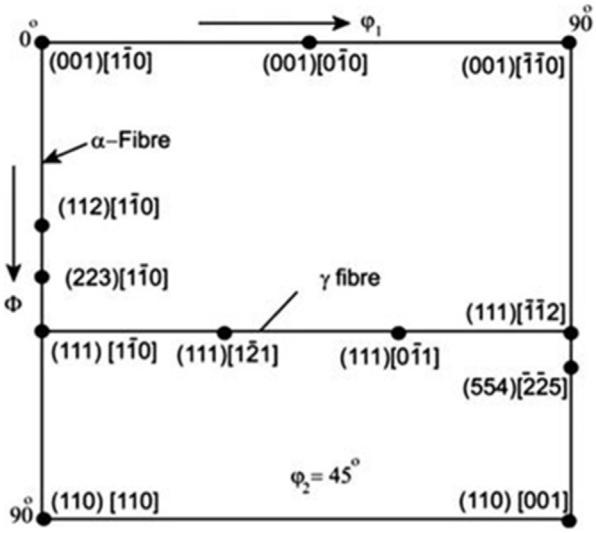

FIGURE 3
Orientations of the standard BCC texture at the ϕ_2 = 45° section. Reproduced with permission (Suwas et al., 2014).

a ϕ2 angle of 45°. The RD fiber extends from (001) ⟨110⟩ to (111) ⟨110⟩ in the φ_1 direction, whereas the ND fiber extends from (111) ⟨110⟩ to (111) ⟨112⟩ along the φ_1 direction (Suwas et al., 2014).

3 Microstructural classes and texture mechanisms in medium manganese steels

3.1 Ferritic medium manganese steels (3–6 wt% Mn)

Ferritic MMnSs multi-phase microstructures exhibit distinct microstructural characteristics, primarily featuring an α ferrite matrix with dispersed retained or reverted γ austenite. The low

Mn content stabilizes the ferrite phase, while small amounts of austenite are retained due to carbon partitioning during the intercritical annealing process. This ferritic matrix contributes to high yield strength and dimensional stability; however, it presents limited ductility unless aided by the TRIP effect attributable to austenite. Regarding texture development, ferritic MMnSs show pronounced cube ({001}//ND) and α fiber ({110}//RD) orientations (Jia et al., 2017). It was observed that cube texture becomes dominant post-intercritical annealing, with α fiber textures developing primarily during the rolling process. Although the minor γ austenite fraction introduces weak γ fiber ({111}//RD) orientations, its overall influence is substantially lower than that observed in duplex steels (Song et al., 2018). Mechanistically, dislocation slip serves as the primary mode of deformation due to moderate SFE. The TRIP effect enhances ductility as retained austenite transforms into martensite under stress. Additionally, the texture stability in ferritic MMnS is notably high, as ferrite demonstrates resistance to reorientation during deformation processes. In terms of applications, ferritic MMnSs are well-suited for scenarios demanding high yield strength and dimensional stability. However, their design makes them less favorable for deep drawability, primarily due to the limited strengthening provided by the γ fiber orientations. Ferritic MMnSs are dominated by an α-ferrite matrix with dispersed retained or reverted γ-austenite. The relatively low Mn content stabilizes ferrite, while small fractions of austenite are retained through carbon partitioning during intercritical annealing. The ferritic matrix provides high yield strength and dimensional stability, but ductility is limited unless austenite contributes via TRIP (Zhao et al., 2023).

3.2 Austenitic medium manganese steels (9–12 wt% Mn)

Austenitic-MMnSs are characterized by a predominant γ austenitic structure, stabilized thermodynamically by high Mn and Ni content, with carbon partitioning during annealing further enhancing this stability (Cai et al., 2016; Zhang et al., 2020). The SFE within these steels are at levels that effectively inhibit martensitic transformation while allowing for mechanical twinning, which plays a crucial role in the material's mechanical behavior (Wang et al., 2023). These steels are noted for developing robust γ fiber textures, specifically aligned along the {111} direction relative to the rolling direction (RD). Researchers have established that mechanical twinning aids in the reorientation of grains toward {111} and {110} orientations, thereby strengthening the γ fiber and significantly contributing to enhanced ductility (Xu et al., 2025). Furthermore, EBSD studies have shown that TWIP is a dominant mechanism in the texture evolution of these materials. Key mechanistic insights include the TWIP effect, which refers to how mechanical twinning reinforces the γ fiber; the influence of high SFE owing to the presence of Mn, Ni, and carbon, promoting slip and twinning instead of martensitic transformation; and the dynamic evolution of texture, where the γ fiber becomes more pronounced with increasing strain, leading to improved formability. From a practical perspective, austenitic MMnSs are particularly suited for applications necessitating exceptional ductility and formability. However, their significant manganese content raises production costs, and their overall strength remains lower compared to duplex steels, suggesting a trade-off between ductility benefits and economic factors alongside strength considerations (Liu et al., 2018). Austenitic-MMnSs are fully or predominantly γ-austenitic. High Mn and Ni contents stabilize austenite thermodynamically, while carbon partitioning during annealing further enhances stability. These steels exhibit SFE in the range that suppresses martensitic transformation but permits mechanical twinning.

3.3 Duplex medium manganese steels (6–9 wt% Mn)

Duplex-MMnSs feature a dual-phase structure comprising balanced amounts of ferritic and austenitic phases. The process of intercritical annealing facilitates carbon partitioning into the austenite phase, resulting in fine reverted γ networks embedded within the ferrite matrix (Varanasi et al., 2022). This specific microstructure fosters both TRIP and Twinning-Induced Plasticity TWIP mechanisms to operate simultaneously, augmenting overall mechanical performance (Zhang et al., 2022). In terms of texture development, duplex MMnSs exhibit intricate textural characteristics. The ferritic phase develops orientations aligned with cube and α fibers, while the reverted austenite phase fortifies the γ fiber orientations. Additionally, twinning within the austenite introduces new components along the {111} and {110} directions. These synergistic textures in duplex steels contribute to a favorable balance of strength and ductility, positioning them as superior choices within the category of high-performance materials (Lee et al., 2018). Mechanistically, the TRIP effect leads to the transformation of austenite into martensite, which significantly boosts the material's strength (Li et al., 2024). Conversely, the TWIP effect entails grain reorientation through twinning, enhancing ductility (Bai et al., 2021). Furthermore, the synergy between the textures of the ferrite and austenite phases offers isotropic properties alongside improved formability, crucial for numerous applications. The implications of these characteristics underscore the significance of duplex MMnSs in automotive applications. They achieve remarkable tensile strength due to the presence of ferrite and martensite while ensuring sufficient ductility via austenite and twinning phenomena. The complexity of texture evolution within duplex steels serves to provide the most advantageous mechanical properties, solidifying their role as a technologically relevant class of materials in modern engineering.

4 Role of alloying elements in texture development

4.1 Influence of manganese (Mn)

Mn promotes γ-fiber ({111}//RD) strengthening, enhancing ductility and formability. In duplex steels, Mn ensures sufficient austenite fraction to balance ferritic cube orientations. Mn plays crucial roles in the development of texture in medium-Mn steels, influencing various key aspects. It enhances the stability of γ-austenite by lowering the SFE, which delays martensitic transformation and facilitates TRIP and TWIP during deformation (Grajcar et al., 2018). The maintenance of γ-fiber texture is essential for achieving high ductility and toughness in these materials. The content of Mn significantly affects recrystallization

TABLE 2 Influence of manganese content on texture evolution, microstructural stability, and resulting strength–ductility balance in MMnSs.

Mn content	Texture effect	Microstructural impact	Mechanical consequence
Low (<5 wt%)	Weak γ-fiber, faster recrystallization	Limited retained austenite	Higher ductility, lower strength
Medium (6–10 wt%)	Strong γ-fiber + cube textures	Stable retained austenite, balanced TRIP/TWIP	Optimal strength–ductility balance
High (>12 wt%)	Excess γ-fiber, delayed recrystallization	Segregation, risk of brittle phases	High strength, reduced toughness

and deformation textures; notably, steels with 6–10 wt% Mn exhibit distinct differences in deformation kinetics and texture development compared to those with lower Mn concentrations (Singh et al., 2023). Higher Mn levels disrupt the equilibrium between ferrite and austenite, leading to variations in orientation distribution and grain boundary character. Moreover, Mn promotes austenite reversion during intercritical annealing, influencing both the morphology and orientation of the reverted austenite, with the initial microstructure and Mn content playing a critical role in the kinetics of this reversion and the uniformity of the resulting texture (Zuo et al., 2026). At elevated concentrations, Mn enhances SFE, which encourages twinning, while at moderate concentrations, it balances TRIP and TWIP mechanisms, thereby refining the texture. Additionally, Mn alters the proportion of coincidence site lattice (CSL) boundaries, which contribute to improved mechanical performance and corrosion resistance. The document also highlights the synergistic interaction of Mn with aluminum and silicon, which refines bainitic/ferritic matrices and stabilizes retained austenite. However, excessive Mn may compromise corrosion resistance due to segregation issues (Mohapatra et al., 2026c). The study underscores the importance of predictive modeling that comprehensively incorporates Mn's influence on TRIP and TWIP in texture evolution models. Optimizing Mn content is deemed necessary for achieving a balance among mechanical strength, ductility, and corrosion resistance (Mohapatra et al., 2023d). Furthermore, pilot trials are recommended to validate the role of Mn in texture retention during processes like continuous annealing and hot press forming. In summary, manganese is vital for enhancing the mechanical properties of MMnSs while requiring careful management to avoid potential downsides related to corrosion resistance. The effect of manganese alloying on texture evolution and mechanical response is presented in Table 2.

4.2 Effect of nickel (Ni)

Ni plays a crucial role in the development of material texture, primarily through its effects on austenite stabilization, grain refinement, orientation control, and slip system activation (Cen et al., 2022). During intercritical annealing, Ni preferentially partitions into austenite, which increases its stability. This process enhances the fraction of RA, effectively delaying the martensitic transformation and fortifying the TRIP and TWIP mechanisms. The addition of Ni leads to finer grains in both ferrite and austenite. This refinement reduces texture heterogeneity and promotes the critical γ-fiber texture, oriented as ⟨111⟩//ND, which is essential for enhancing ductility and toughness (Xia et al., 2020). Steels containing Ni exhibit improved activation of slip systems in both FCC austenite and BCC ferrite phases (Kumar et al., 2025a). This augmentation enhances the strain hardening response, allowing for greater uniform deformation and delaying necking during mechanical stress. The behavior of Ni in partitioning contributes to austenite stability and suppresses premature transformations (Zhang et al., 2020). More stable RA enhances the TRIP effect, leading to improved elongation in the material. Additionally, Ni facilitates the formation of twin boundaries and increases γ-fiber intensity, linking microstructural characteristics with tensile properties. Even small additions of Ni (approximately 1 wt%) can yield performance benefits that surpass those of higher Mn steels in terms of the strength-ductility balance (Kumar et al., 2023). The significant role of Ni in promoting γ-fiber texture and twin boundaries is vital for tailoring the anisotropy of sheet steels (Kumar et al., 2025a). The properties imparted by Ni in comparison to high-Mn steels mitigate risks of banding and segregation, making Ni-containing steels more desirable for various applications such as welding and forming, thus highlighting its industrial relevance. Comparative impact of nickel content on texture development, microstructural refinement, and mechanical performance in MMnSs is shown in Table 3.

4.3 Role of carbon (C)

During intercritical annealing, carbon preferentially diffuses into austenite which stabilizes the retained austenite at room temperature (Li Y. et al., 2017). This process enriches austenite, promoting a γ-fiber texture ({111} that later transforms into advantageous orientations in ferrite post-deformation. A higher carbon content also delays the recrystallization of ferrite, allowing deformation textures to persist for extended periods (Aliabad et al., 2025). Carbon plays a critical role in the kinetics of cementite precipitation and dissolution when combined with manganese. Fine cementite particles help pin grain boundaries, which slows down recrystallization and sharpens the resulting texture (Lamari et al., 2026). During annealing, the controlled dissolution of cementite releases carbon back into the austenite, thereby enhancing the uniformity of the texture. In medium-Mn steels, carbon influences the driving force for the transformation of martensite back to austenite upon heating. This transformation is significant as it leads to the development of cube and Goss textures in reverted austenite, which subsequently impact mechanical anisotropy. While carbon in solid solution increases strength, it can also diminish toughness if austenite levels are insufficient. Notably, studies have indicated that higher carbon levels can enhance Charpy impact performance by stabilizing increased amounts of retained austenite (Kwok et al., 2023; Mohapatra et al., 2024b). This stabilization is correlated with favorable texture components, helping resist brittle fracture. It is also noted that excess carbon can

TABLE 3 Effect of nickel content on texture evolution, microstructural refinement, and strength–ductility balance in MMnSs.

Ni content	Texture effect	Microstructural impact	Mechanical consequence
0 wt%	Weaker γ-fiber, less RA stability	Coarser grains, heterogeneous texture	Lower ductility, unstable TRIP
~1 wt%	Strong γ-fiber, refined grains	Stable RA, enhanced twin boundaries	Excellent strength–ductility synergy
>2 wt%	Excess stabilization, risk of cost issues	Over-refined grains, reduced TRIP efficiency	High ductility, but less economical

TABLE 4 Effect of carbon content on texture evolution, retained austenite stability, and the resulting strength–ductility balance in medium-Mn steels.

Carbon level	Texture effect	Microstructural impact	Mechanical consequence
Low (<0.1 wt%)	Weak γ-fiber, faster ferrite recrystallization	Limited retained austenite	Higher ductility, lower strength
Medium (0.15–0.3 wt%)	Balanced γ-fiber and cube textures	Stable retained austenite, controlled cementite	Good strength–ductility balance
High (>0.3 wt%)	Strong γ-fiber, delayed recrystallization	Excess carbon segregation, risk of carbide networks	High strength, reduced toughness

lead to carbide networks that reduce toughness and disrupt texture uniformity, while insufficient carbon results in unstable austenite, weak γ-fiber texture, and poor transformations associated with TRIP and TWIP effects (Aliabad et al., 2025). An optimal carbon content in the range of approximately 0.2–0.3 wt% is generally preferred for automotive-grade MMnSs, providing a balance between texture sharpness and overall mechanical performance. Comparative influence of carbon content on texture evolution, retained austenite stability, and the resulting strength–ductility balance in MMnSs is shown in Table 4.

4.4 Influence of aluminum (Al)

Ferrite stabilization is significantly influenced by the presence of aluminum, which acts as a strong ferrite stabilizer, counterbalancing manganese's austenite-stabilizing effect (Sripushpa et al., 2026). This interaction effectively shifts the intercritical annealing window upwards, impacting the fraction and orientation of RA. EBSD studies have demonstrated that aluminum promotes a cube texture ($\{001\}\langle 100\rangle$) in ferrite, a feature that enhances isotropy in mechanical properties (Ridlo et al., 2025). In terms of carbide suppression, aluminum plays a crucial role by reducing cementite precipitation through the lowering of carbon activity. This suppression prevents the formation of carbide networks, resulting in cleaner grain boundaries and sharper texture components (Lin et al., 2026). Consequently, this leads to a more uniform γ-fiber ($\{111\}$) texture in austenite, thereby enhancing its ductility. Aluminum additions also affect recrystallization and annealing behavior. They delay the recrystallization of ferrite, allowing deformation textures to be preserved for longer durations (Ridlo et al., 2025). Within the temperature range of 650 °C–675 °C during intercritical annealing, aluminum-containing steels exhibit a favorable balance between strength and ductility. However, temperatures exceeding this range can destabilize austenite, resulting in martensite formation and degradation of texture. The impact of aluminum on mechanical properties is characterized by an improvement in low-temperature toughness due to grain size refinement and a shift in temper embrittlement to higher temperatures (approximately from 300 °C to 350 °C) (Lin et al., 2026). This relationship correlates with texture evolution; the refined ferrite grains with cube orientation diminish the risk of cleavage fractures. Conversely, inadequate aluminum content can lead to carbide precipitation, compromising toughness and rendering textures less stable, while excessive aluminum can excessively stabilize ferrite, reduce the amount of retained austenite, and adversely affect TRIP and TWIP effects. The optimal range of aluminum concentrations—approximately 0.2 to 0.3 wt%—strikes a balance between γ-fiber and cube textures, effectively suppresses carbides, and enhances toughness, making it particularly suited for automotive applications (Mohapatra et al., 2025a). Influence of aluminum content on texture evolution, carbide suppression, and the resulting strength–ductility balance in MMnSs is shown in Table 5.

4.5 Effect of silicon (Si)

Silicon plays a crucial role in inhibiting the precipitation of cementite during intercritical annealing, which allows for a higher retention of carbon in solution within the austenite phase (Mohapatra et al., 2025a). This process stabilizes the austenite and enhances the γ-fiber texture, specifically the ($\{111\}$) orientation. Improved grain boundaries resulting from Si addition lead to sharper and more uniform texture properties in the steel. By enabling the retention of carbon within austenite, Si contributes indirectly to its stabilization, which is critical for the TRIP effect. As retained austenite transforms under strain, it enhances ductility and facilitates the evolution of texture in the material. The addition of silicon delays the recrystallization of ferrite, allowing for longer preservation of deformation textures (Pierce et al., 2015). EBSD studies indicate that silicon fosters optimal cube ($\{001\}\langle 100\rangle$) and γ-fiber textures, achieving a favorable balance between strength and ductility. In MMnSs, silicon functions synergistically with manganese (which stabilizes austenite) and aluminum (which stabilizes ferrite). This cooperative action helps control phase fractions and texture components, thereby minimizing anisotropy in mechanical properties. Notably, insufficient silicon content can lead to undesirable carbide precipitation and an unstable austenite phase, while excessive silicon can cause segregation, brittleness,

TABLE 5 Effect of aluminum content on texture evolution, carbide suppression, and the resulting strength–ductility balance in medium-Mn steels.

Al content	Texture effect	Microstructural impact	Mechanical consequence
0 wt%	Strong γ-fiber, faster recrystallization	Higher carbide precipitation	Good ductility, lower toughness
~0.25 wt%	Balanced γ-fiber + cube textures	Suppressed carbides, refined ferrite	Improved toughness, stable retained austenite
>0.5 wt%	Excess ferrite stabilization, weaker γ-fiber	Risk of insufficient austenite stabilization	Reduced ductility, higher brittleness

TABLE 6 Impact of silicon content on texture effect, carbide suppression, and the resulting mechanical response in MMnSs.

Si content	Texture effect	Microstructural impact	Mechanical consequence
0 wt%	Strong carbide precipitation, weaker γ-fiber	Reduced retained austenite	Lower ductility, poor TRIP effect
~0.2–0.5 wt%	Balanced γ-fiber + cube textures	Suppressed carbides, stable austenite	Good strength–ductility balance
>1 wt%	Excess suppression, delayed recrystallization	Risk of brittle phases, segregation	Reduced toughness, anisotropy

and significant delays in recrystallization (Ma et al., 2026). The optimal silicon concentration is identified as being in the range of approximately 0.3–0.5 wt%, which effectively suppresses carbide formation, stabilizes austenite, and enhances the desirable γ-fiber texture for automotive-grade steel applications. Influence of silicon content on texture evolution, carbide suppression, and the resulting strength–ductility balance in MMnSs is shown in Table 6.

The collective influence of Mn, Al, C, Si, and Ni on phase stability, stacking fault energy, and austenite reversion ultimately governs the strength–ductility balance that defines the performance of advanced high-strength steels. Stable and finely dispersed reverted austenite, promoted by Mn, Ni, and C, provides a sustained TRIP effect, enhancing ductility without sacrificing strength. Simultaneously, controlled reductions in SFE through Al and Si enable twinning-induced plasticity, which augments strain hardening capacity and delays necking. The synergy between these mechanisms ensures that steels can achieve high yield strength from ferritic and martensitic matrices while maintaining exceptional elongation through transformation and twinning pathways. Texture evolution further reinforces this balance, with γ-fiber strengthening improving formability and cube orientations contributing to isotropy. Thus, alloying design serves as a strategic tool to engineer microstructures that harmonize strength and ductility, positioning medium-Mn steels as a cornerstone in the development of next-generation automotive and structural materials.

5 Texture evolution associated with mechanical properties

Texture-induced anisotropy significantly influences the deep drawability and formability properties, YS, and elastic modulus of BCC steels (Xie and Nakamachi, 2002; Raabe, 1997). The properties are enhanced by the ND or γ-fiber present in the ferrite phase, whereas cleavage fractures are propagated by the (001) planes in BCC materials (Ghosh et al., 2014). Delamination behavior is adversely affected by the cube fiber texture, specifically the (001) < 110> orientation (Ghosh et al., 2016). Thus, it is more advantageous to deduce from previous research that the formation of cube fibers should be limited to achieve superior tensile properties (Mohapatra et al., 2024a). The YS is reportedly enhanced when the transformation texture contains a greater proportion of fiber in the (113) < 110> orientation, which is a substantial constituent of RD//<110> fiber (Hutchinson et al., 2005). Like the BCC phase, the tensile properties are significantly influenced by the textural components of the FCC phase. (Barbier et al., 2009) explained that superior tensile properties can be achieved by incorporating the texture intensities of brass components into high-manganese TWIP steel during deformation. However, MMnS exhibits distinct characteristics. The following studies examine the evolution of texture and its correlation with the tensile behavior of MMnS (Table 7).

5.1 Effect of annealing temperature

It was reported that α-fiber in the FCC phase remains unchanged after the tensile deformation in intercritically annealed Fe-6.78Mn-3.92Al-0.18C (wt%) MMnS samples (Mohapatra et al., 2023e). The orientation distribution function (ODF) represents the texture components of the samples. The pre-tensile ODFs of A_700, A_750, and A_800 samples (annealed at 700, 750, and 800 °C, respectively) are displayed in Figure 4. More recrystallization and independent orientations resulted from decreased textural-component intensity as annealing temperature increased. All the annealed samples exhibit significant α-fiber, resulting in randomly oriented grains and reduced cube components (Mohapatra et al., 2024c).

All the deformed samples have substantial α-fiber components, notably Ms brass and Goss/brass twin (Figure 5). Deformed samples have strong Cu and S components. Nevertheless, the primary constituent of the texture, Ms brass {011} ⟨211⟩, partially shifted towards the Goss/brass twin {011} ⟨111⟩ component, exhibiting the TRIP effect when subjected to tensile deformation.

5.2 Effect of cold rolling on texture

Figure 6 illustrates the initial microstructures of the experimental cold-rolled (CR) steel before tensile deformation. Red and green contrasts, respectively, represent the BCC and FCC

10.3389/fmats.2026.1954859

TABLE 7 Showing MMnS compositions and processing conditions versus texture components and mechanical properties.

Composition	Processing conditions	Texture components	Mechanical properties	References
Fe-4.9Mn - 0.18C-0.8Si-0.4Al	CR (~73% red.) + IA 640 °C/2 h (globular) vs. Homogenization 850 °C/20 min + WQ + IA 640 °C/2 h (lamellar)	Bulk texture determined for ferrite and austenite (CMWP/EBSD analysis); CMWP dislocation density calculated	YS: *NA* UTS: *NA* TE: *NA* (Study focused on EIS and potentiodynamic polarization in 3.5% NaCl)	(Kishore et al., 2023)
Fe-5Mn - 0.18C-0.80Si-0.40Al	Cold Rolling + IA (640 °C for 2 h); tested at Quasi-static (10^{-4} s^{-1}) vs. Dynamic (200 s^{-1}) rates	Quasi-static: Brass {110}⟨112⟩ and rotated Goss {110}⟨110⟩ in FCC; BCC {111} γ-fiber Dynamic (200 s^{-1}): Transitions to Copper {112}⟨111⟩, S {123}⟨634⟩, and P {011}⟨233⟩ via adiabatic heating	Quasi-static: YS ~994 MPa, UTS ~1,147 MPa, TE 38.8%, PSE 44.5 GPa·% Dynamic: TE increases by ~12% (delayed necking)	(Alam et al., 2026)
Fe-5Mn - 0.35C-3.2Al	Forging + Hot Rolling (880 °C, 7 mm) + Intercritical Annealing (750 °C) vs. Double IA (DIA)	NA (Quantitative ODF texture components not evaluated; *in situ* high-energy XRD micromechanical loading partitioning and PLC bands reported)	IA: UTS 777.1 MPa, TE 39.6%, PSE 30.8 GPa·% DIA: UTS 953.6 MPa, TE 59.1%, PSE 56.4 GPa·% YS: NA	(Mao et al., 2024)
Fe-5.6Mn - 1.1Al-0.2C and Fe-5.6Mn - 1.1Al-0.2C-0.1Ti-0.22Mo	Hot Rolling + Cold Rolling (2 mm) + Superplastic Tensile Testing at 685 °C–775 °C	ODF φ_2 = 45°: α-fiber (<110>//RD), weak {112}<110> and {111}<110> in α/α'; randomizes during superplastic deformation (GBS)	YS: *NA* UTS: *NA* (High-temp superplastic elongation up to 1,170% at 745 °C reported; Vickers hardness ~280–450 HV)	(Zhang et al., 2023)
Fe-6Mn - 0.14C-0.23Si	Cold Rolling + Batch Annealing at 620 °C (air cooling)	Pole figures {100}, {110}, {111} for ferrite and austenite (preferred orientation observed, anisotropic Lüders strain)	YS: *NA* (Lüders strain YPE = 9.5% reported) UTS: 1,012 MPa TE: 42.3%	(Wang et al., 2019)
Fe-6Mn - 0.3C-3.0Al-1.5Si (IA at 760 °C)	Hot rolling + Intercritical Annealing (IA) at 760 °C for 10 min	Undeformed ferrite {100}⟨011⟩; post-tensile ferrite α-fiber {100} and weak γ-fiber {111}. Austenite undeformed Brass and Goss; post-tensile Brass and Cu components. Coarse δ-ferrite + UFG (α+γ) bands	YS: 788 MPa UTS: 925 MPa TE: 49.5% PSE: 45.8 GPa·%	(Choi et al., 2017)
Fe-6Mn - 0.3C-3Al-1.5Si (IA at 800–880 °C)	Hot rolling + IA at 800 °C, 840 °C, or 880 °C for 10 min	Layered bimodal structure; higher strain-induced α′ martensite transformation (up to 73%). Ferrite/austenite ODF components as above	800 °C: YS 700 MPa, UTS 985 MPa, TE 47% 840 °C: YS 700 MPa, UTS 1130 MPa, TE 35% 880 °C: YS 515 MPa, UTS 1365 MPa, TE 19.3%	(Choi et al., 2017)
Fe-6.2Mn - 0.12C-1.4Cu-0.93Ni-1.40Si (CR Route)	Hot Rolling (HR) (4.3 mm) + Cold Rolling (1.5 mm) + ART Annealing (600 °C–640 °C) [Initial state: Cold-rolled martensite]	FCC ODF (ϕ_2 = 45°): Peak between Goss {110}⟨001⟩ and Brass {110}⟨112⟩, weak Cu {112}⟨111⟩; strong BCC γ-fiber (⟨111⟩∥ND). Nano Cu-rich particles (<20 nm), 16.8% annealing twin grains	YS: 994–1,036 MPa UTS: 1,147–1,196 MPa TE: 38.8%–48.5% PSE: 44.5–58.0 GPa·%	(Yan et al., 2019)

(*Continued*)

10.3389/fmats.2026.1954859

TABLE 7 Continued

Composition	Processing conditions	Texture components	Mechanical properties	References
Fe-6.83Mn - 0.22C-1.53Si (IA and Q&P Treatment)	Cold rolled (1.2 mm) + Intercritical Annealing (640, 660, 680 ℃ for 600 s) + Quenched to 75 ℃ + Partitioned at 450 ℃ for 60 s	Ferrite + martensite + retained austenite (lamellar γL and equiaxed γE) Ferrite ODF: E {111}⟨110⟩, B {011}⟨112⟩ Austenite ODF: B {011}⟨211⟩, G {110}⟨001⟩, C {112}⟨111⟩	IA640: YS ~1,000–1,100 MPa, UTS ~1,100 MPa, TE ~27% IA660: YS ~1,180 MPa, UTS ~1,180 MPa, TE ~25% IA680: YS ~920 MPa, UTS ~1,150 MPa, TE ~14%	(Yang et al., 2018)
Fe-7Mn - 0.18C-4Al-1.34Si	Hot forging + Hot rolling (1,100 ℃, 80% red.) + IA at 700 ℃ and 800 ℃ for 1 h	IA _700: Strong α-fiber with dominant Brass at ~(110); higher Cube {001}⟨100⟩ component; RA fraction ~21.4% IA _800: Ms Brass shifts towards Goss and Cu components; weakened Cube texture due to grain growth. RA fraction ~32.2%	IA _700: YS: 757 MPa UTS: 757 MPa TE: 34% PSE: ~25.7 GPa·% (TRIP ratio 61%) IA _800: YS: 771 MPa UTS: 771 MPa TE: 43% PSE: ~33.2 GPa·% (TRIP ratio 71%)	(Mohapatra et al., 2024d)
Fe-7Mn - 0.3C-3.5Al	Warm Rolling (WR) + Inter critical Annealing (IA) at 775 ℃	Quantitative ODF components; dynamic recrystallized equiaxed dual-phase microstructure reported	YS: *NA* UTS: *NA* Superplastic TE: 1,401% (at 775 ℃, strain rate 5×10^{-4} s^{-1})	(Pan et al., 2023b)
Fe-7Mn - 0.3C-3.5Al	Hot Rolling (80% red.) + Cold Rolling (80% red.) + HTTT at 800 ℃ across strain rates (5×10^{-4} to 2.5×10^{-2} s^{-1})	5×10^{-3} s^{-1}: Texture randomized (peak drops from 6.73 to 2.45) due to GBS dominance 2.5×10^{-2} s^{-1}: HSRS via Rachinger sliding + DRX; 44% RA content	YS: *NA* UTS: *NA* Superplastic TE: 1,157% at 5×10^{-3} s^{-1} (m = 0.6); 322% at 2.5×10^{-2} s^{-1} (m = 0.43) PSE: *NA*	(Pan et al., 2023c)
Fe-7.23Mn - 0.09C-4.42Al-1.99Si-0.5Cu (A0: 0% pre-strain) Fe-7.23Mn - 0.09C-4.42Al-1.99Si-0.5Cu (A2: 2% pre-strain)	HR + Annealing (750 ℃, 5 h) + CR (1.5 mm) + 0% pre-strain + Q and P (750 ℃ 20 min → 25 ℃ 90s → WQ)	Multiphase martensite, α-ferrite, δ-ferrite, retained austenite. Higher ⟨111⟩ texture, lower ⟨001⟩ and ⟨101⟩. Lath-like retained austenite Refined multiphase structure; stronger ⟨111⟩ and ⟨101⟩ orientations. 73.8% large-angle grain boundaries. Blocky/granular retained austenite stabilized by C/Mn	YS: *NA* UTS: 896 MPa TE: 34.72% PSE: 31.10 GPa·% YS: *NA* UTS: 902 MPa TE: 39.28% PSE: 35.43 GPa·%	(Wu et al., 2023)
Fe-9.35Mn - 0.22C-7.19Al-1.12Si-0.03Ti (A2: Ti-modified) Fe-9.80Mn - 0.2C-7.50Al-1.22Si (A1: Ti-free)	Forged + HR + CR (50% red. to 2 mm) + Salt bath annealed at 1073 K (800 ℃) for 3 min or 50 min	Duplex ferrite + austenite with Ti-rich intermetallic carbides (~15–35 nm) + $Mn_5(Si,Al)C$. Ferrite γ-fiber and Cube fiber evolution governed by Taylor factor M distribution (~2–5) Ti free Duplex ferrite + austenite with $Mn_5(Si,Al)C$ precipitates (150–300 nm) Ferrite ODF: γ-fiber ({111}⟨110⟩ to {111}⟨112⟩), Cube fiber ({001}⟨110⟩ to {001}⟨010⟩) Austenite ODF: α-fiber (Goss to Brass)	A2-3min: YS ~880 MPa, UTS ~1,020 MPa, TE ~18% A2-50min: YS ~870 MPa, UTS ~980 MPa, TE ~28% A1-3min: YS ~910 MPa, UTS ~1,130 MPa, TE ~25% A1-50min: YS ~810 MPa, UTS ~920 MPa, TE ~12%	(Sarkar et al., 2019)

(*Continued*)

TABLE 7 Continued

Composition	Processing conditions	Texture components	Mechanical properties	References
Fe-10.86Mn - 2.2Al-1.8Si-0.22C	60% Cold Rolling + Intercritical Annealing (800 °C for 30 min)	Residual < 101> austenite texture retained after CR; orientation randomization increases after IA with decrease in K-S relationship	YS: NA UTS: NA TE: NA (PSE ≥60 GPa·% cited; *in-situ* EBSD grain refinement mechanisms)	(Liu et al., 2025)
Fe-11.2Mn - 0.2C-1.95Al	Cold rolling (1 mm) + Controlled Annealing (600 °C–750 °C, 5 min–48 h)	Ferrite grains with strong γ-fiber ({111}‖ND) and α-fiber. γ-fiber intensity increases with soaking time	YS: ~600–880 MPa UTS: ~1,000–1,350 MPa TE: > 30% PSE: > 30 GPa·% (Yield Point Elongation YPE suppressed via γ-fiber)	(Cai et al., 2019)

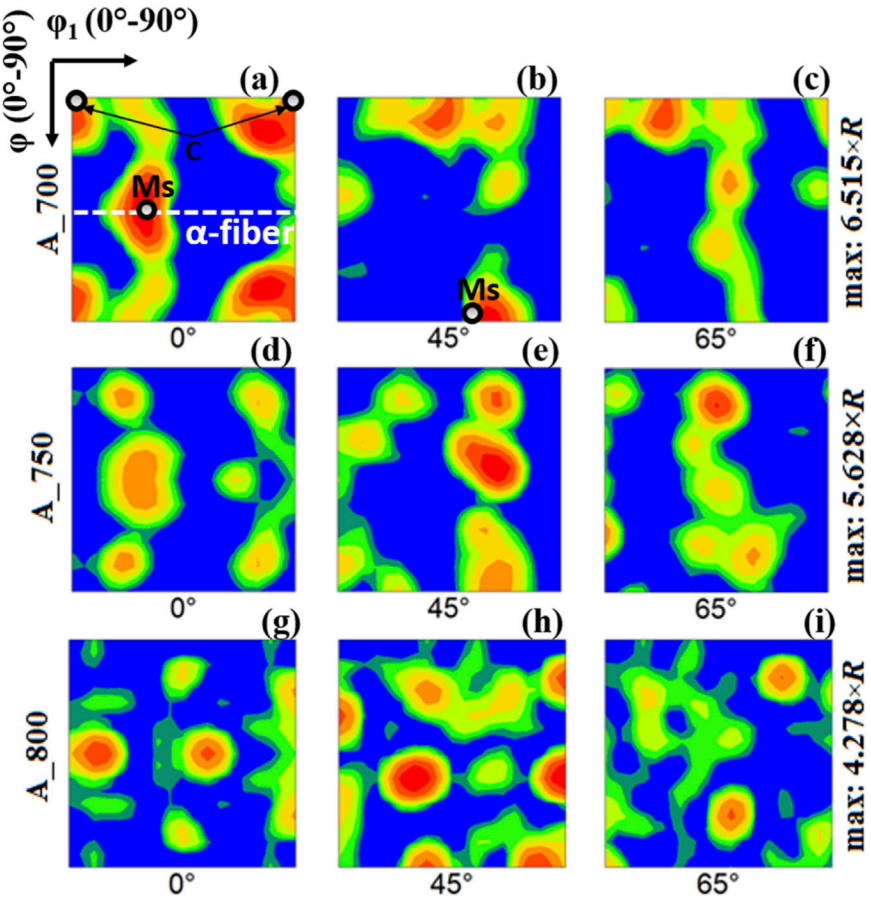

FIGURE 4
Orientation distribution function (ODF) sections of FCC-austenite in the annealed samples before tensile deformation at φ_2 = 0° **(a,d,g)** 45° **(b,e,h)** and 65° **(c,f,i) (a–c)** A_700, **(d–f)** A_750, and **(g–i)** A_800. Important textural components are shown in Fig. 19(c) cube {001} ⟨100⟩; Ms, MS brass {011} ⟨211⟩; α-fiber {011}//ND. Adopted with permission (Mohapatra et al., 2023e).

phases. White and black lines indicate low-angle grain boundaries (LAGBs) (2°–15°) and high-angle grain boundaries (HAGBs) (≥15°), respectively (Figure 6a). The microstructures of the CR steel primarily consist of α′ martensite, along with a small fraction of retained γ austenite grains (Figure 6a). The average grain size is approximately 0.88 μm. The CR process has introduced a significant amount of deformation energy storage within the microstructure (Figure 6b). Approximately 67% of the grain boundaries are LAGBs, a result of the extensive deformation experienced during the CR process. Furthermore, the ODF indicates that the BCC phase

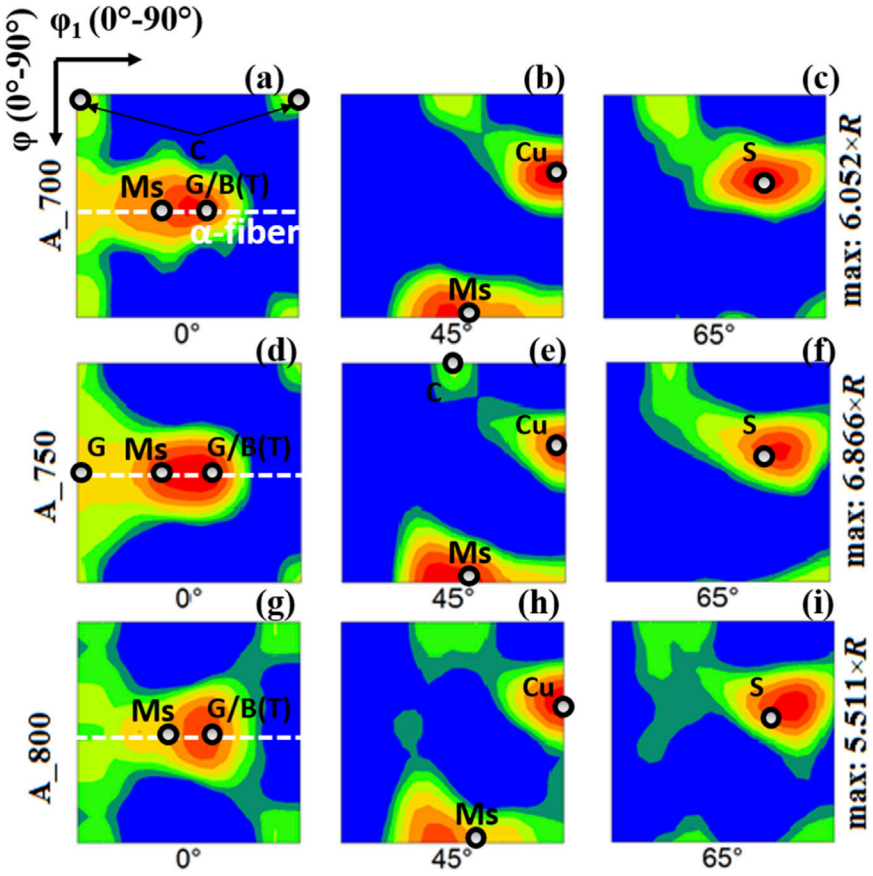

FIGURE 5
ODF sections of FCC-austenite in the deformed samples (after tensile deformation) at φ_2 = 0° **(a,d,g)** 45° **(b,e,h)** and 65° **(c,f,i) (a–c)** A_700, **(d–f)** A_750, and **(g–i)** A_800. Important textural components are shown in Fig. 20(c) cube {001} ⟨100⟩; Ms, MS brass {011} ⟨211⟩; α-fiber {011}//ND; Cu, copper {112} ⟨111⟩; G, Goss {011} ⟨100⟩; G/B (T), Goss/brass twin {011} ⟨111⟩; S, S-component {123} ⟨634⟩. Adopted with permission (Mohapatra et al., 2023e).

exhibits a strong α-fiber orientation along the rolling direction (RD), with a maximum orientation strength of 5.40 (Figure 6c). In contrast, the FCC phase shows a strong {110} orientation with a maximum orientation strength of 17.90 (Figure 6d).

Based on the above tensile results, the samples at the typical temperatures of 700 °C and 750 °C with a true strain of 0.2 were selected to conduct microstructure characterization. The γ content is about 16.7% at 700 °C and 22.2% at 750 °C, which is almost the same when the true strain is 0.9 (Figures 7, 8). This implies that the samples have been completely austenitized before the jump test. During deformation at 700 °C, the average grain size increased by 0.13 μm at 0.9 true strain compared to the initial cold-rolled sheet. Moreover, Figure 7c,d shows that the BCC and FCC phases have distinct textures. It is clear that the initial texture intensity of the two phases is distinct, indicating a change in orientation during deformation. The α-fiber of the BCC phase is enhanced, and the FCC phase is transformed into the brass texture. A change in grain orientation can demonstrate that at high temperatures, materials with such fine microstructure undergo GBS.

Figure 8 illustrates that at a true strain of 0.9 °C and 750 °C, the microstructure of experimental samples underwent significant transformation, with numerous BCC phases converting into FCC phases, leading to an increase in average grain size from 1.01 μm to 1.31 μm. The FCC phase exhibited classic deformation characteristics, with key mechanisms including dynamic recovery and associated fiber evolution from α-fiber {001} to γ-fiber {111}. The FCC phase also developed a brass texture with a maximum orientation strength of 5.72, while {112} nearly vanished, indicating strong superplasticity in the γ-fiber and brass textures (Pan et al., 2023a; Razmpoosh et al., 2020).

5.3 Influence of strain rate on evolution of texture

The influence of strain rate on texture evolution in intercritically annealed Fe-6.78Mn-3.92Al-0.18C (wt%) MMnS has been recently studied (Mohapatra et al., 2023f). A high TRIP effect and austenite transformation ratio (ratio of martensite transformed from austenite during tensile deformation) resulted in a higher low-angle grain boundary (LAGB) fraction in the strained Fe-6.78Mn-3.92Al-0.18C (wt%) steel at lower strain rates (1.33×10^{-4} s^{-1}) (Mohapatra et al., 2025b). Ms brass {011} ⟨211⟩ facilitates the TRIP effect more than other textural components at lower strain rates (1.33×10^{-4} s^{-1}) (Figure 9).

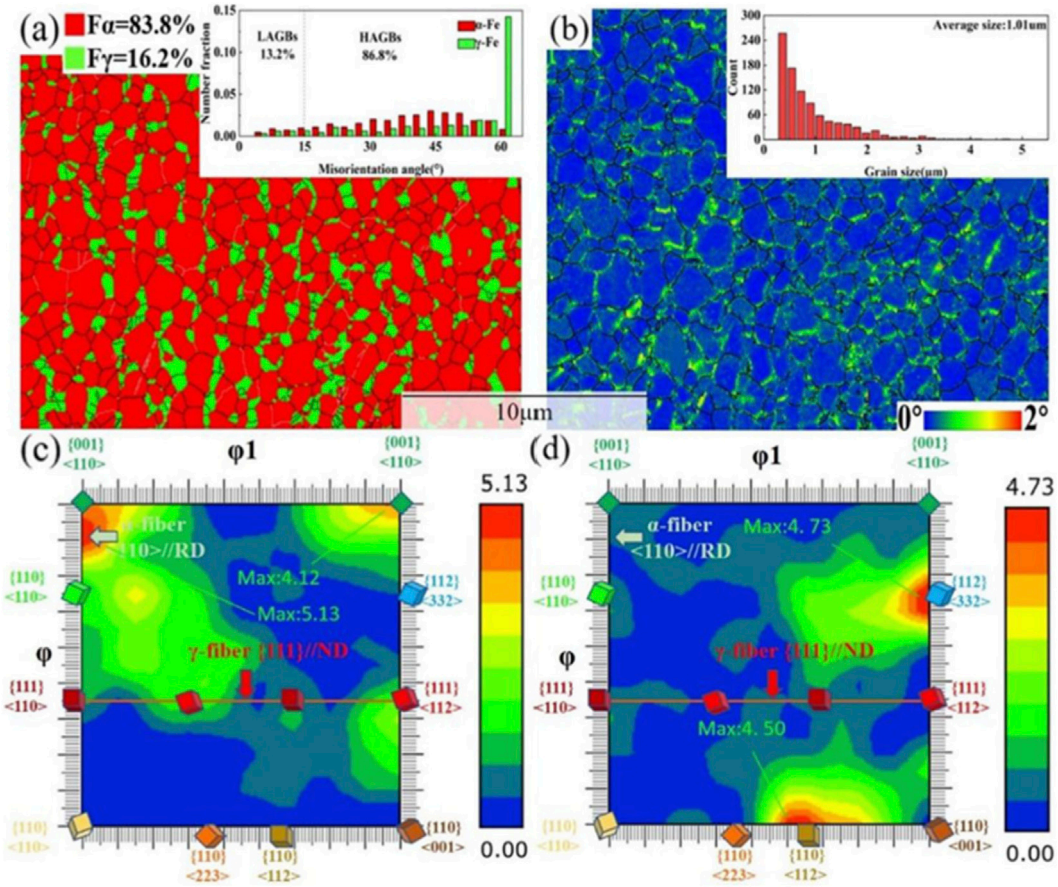

FIGURE 6
Initial microstructure of tensile specimens: **(a)** phase and grain boundaries map, **(b)** kernel average misorientation map and grain size statistics image, **(c)** ODF of the BCC phase, and **(d)** ODF of the FCC phase. Adopted with permission (Pan et al., 2023a).

Recently, researchers investigated the evolution of mesotexture (Patra et al., 2024) specifically focusing on the misorientation angle and axis during the strain-induced martensite transformation under various deformation conditions (Figure 10). The transformation from austenite to α′ martensite adheres to specific crystallographic orientation relationships (OR), particularly the Kurdjumov–Sachs (K–S) type, which is characterized by a misorientation angle of 42.8° around the orientation. Deformations can disrupt the ideal K–S orientation due to grain rotations. Analyzing the distributions of misorientation angles in the deformed samples reveals a consistent and prominent peak at approximately 42.8° across all deformation conditions, indicating successful strain-induced formation of α′ martensite. Samples subjected to a deformation rate of 10^{-3} s^{-1} at room temperature exhibit a sharper peak at this angle with a higher frequency compared to other conditions, suggesting a greater proportion of retained austenite transforming under strain, thus promoting K–S boundary formation. Conversely, at elevated temperatures (409 K) and higher strain rates, the saturation of phase transformation leads to grain rotation, which is necessary to accommodate the deformation, resulting in a deviation from the expected misorientation angle.

Overall, this analysis confirms the crucial influence of deformation parameters on martensitic transformation processes. The sample, which deformed at a strain rate of 10^{-3} s^{-1} at room temperature, exhibits a pronounced peak at 42.8°. This peak is sharper and occurs at a higher frequency compared to other deformation conditions. This phenomenon is attributed to an increased fraction of retained austenite undergoing strain-induced transformation, resulting in boundaries characterized by K–S orientation relationships (OR). Conversely, under conditions of higher strain rates or elevated temperatures, particularly at 409 K, phase transformation reaches saturation. This saturation leads to grain rotation to accommodate deformation, causing deviations from the ideal misorientation angle. Apart from the observed deviation in the misorientation angle, significant changes in the misorientation axis have been recorded during deformation at elevated strain rates. The analysis of the evolution of the misorientation axis with respect to the plastic strain (ε_p) in samples subjected to a strain rate of 10^{-3} s^{-1}, as illustrated in Figure 11a, reveals a notable peak near the direction. This peak intensifies with increasing values of ε_p. Conversely, the results presented in Figure 11b indicate that for samples deformed at a higher strain rate of 10^{3} s^{-1}, the misorientation axis not only shifted towards the [001] direction as ε_p increased but also exhibited a close correlation with the saturation of the phase transformation. This suggests a significant relationship between the evolution of the

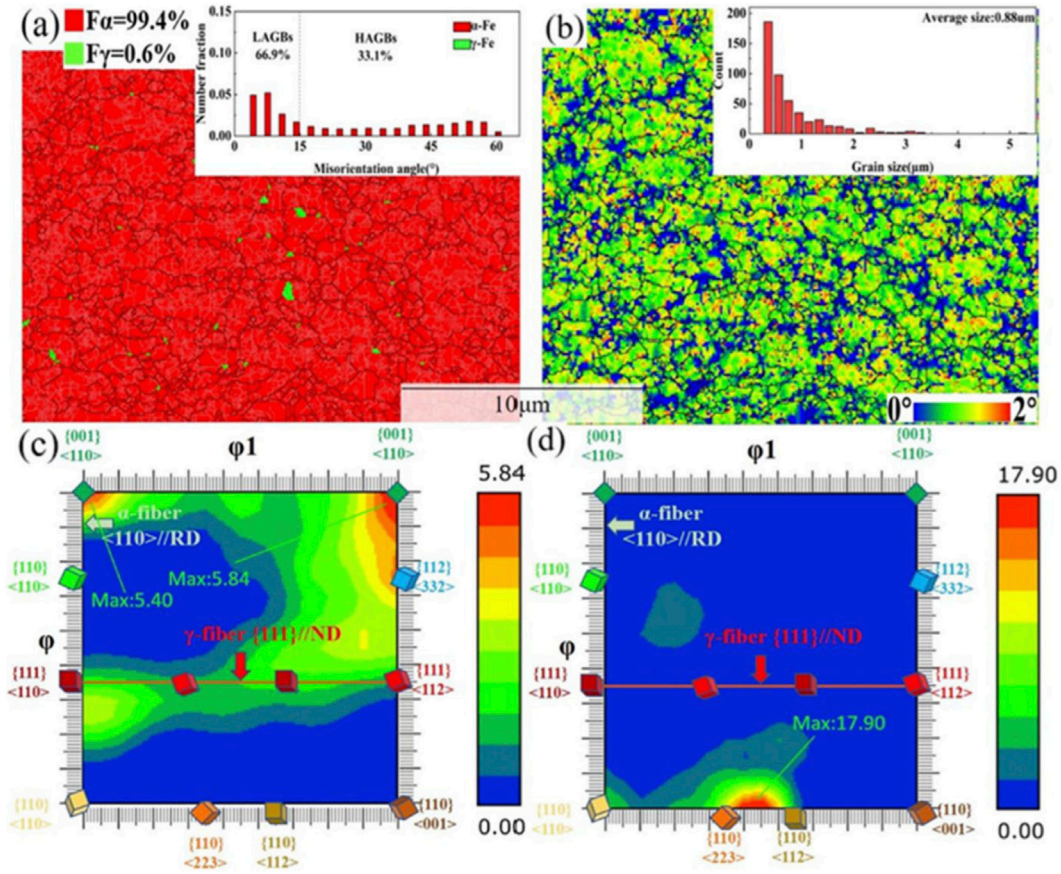

FIGURE 7
Microstructure of HTTT at 700 °C up to 0.9 true strain and strain rate of 1×10^{-3} s^{-1}: **(a)** Phase and grain boundaries map, **(b)** Kernel average misorientation map and grain size statistics image, **(c)** ODF of the BCC phase, and **(d)** ODF of the FCC phase. Adopted with permission (Pan et al., 2023a).

misorientation axis and the deformation conditions in high strain rate scenarios.

The standard ODF section at $\varphi_2 = 45°$ is illustrated in Figure 12a, highlighting important texture components for the BCC phase. The experimental micro-textures for hot-forged (HF) and hot-rolled (HR) specimens are shown in Figures 12b,c, respectively, while the corresponding simulated micro-textures are depicted in Figures 12d,e. The HF specimen exhibits high-intensity Goss {110} and cube texture {001}, with a relatively weaker intensity of {111} also visible in the ODF section at $\varphi_2 = 45°$ (Figure 12b). In contrast, the HR specimen features a rotated-cube texture {001} accompanied by a significantly weakened cube texture {001} (Figure 12c). A comparison between Figures 12b,c reveals that the intensity of the γ-fiber {111}//ND is notably higher in the HR specimen compared to the HF specimen, indicating a difference in micro-textural characteristics.

Moreover, to investigate the influence of strain rates on deformation mechanisms, pole figures for deformed samples are presented (Figure 13). At a strain of $\varepsilon = 0.2$, samples exhibit a similar rolling texture, with peak densities ranging from 6.35 to 6.75. At a strain rate of 5×10^{-4} s^{-1} and $\varepsilon = 0.8$, the texture becomes more concentrated with a peak density of 9.56, suggesting that dislocation slip may be the primary mechanism of deformation. Following significant dislocation slip and creep, small dimensions nucleate and recrystallize. In fractured samples, the peak density drops to 5.46, revealing peaks in multiple directions due to the continuous generation of fine grains, which enhances grain boundary sliding (GBS). At a higher strain rate of 5×10^{-3} s^{-1}, as the strain progresses from $\varepsilon = 0.8$ to fracture, peak density decreases from 6.73 to 2.45, leading to a nearly random texture distribution and indicating that GBS predominantly governs superplastic deformation under these conditions. The behavior at 5×10^{-3} s^{-1} mirrors the previous trend, though the amplitude of variation is slightly less pronounced, further confirming the key role of GBS in high strain rate superplasticity in multi-phase materials.

5.4 Texture associated with fracture characteristics

It is also found that the transverse fracture in intercritically annealed Fe-6.78Mn-3.92Al-0.18C (wt%) MMnS exhibits a higher degree of propagation along the ⟨101⟩ direction as a result of its lower relative intensity (Mohapatra et al., 2024d). Figure 14 shows inverse pole figure (IPF) maps of the (a) BCC and (b) FCC phases, together with the corresponding IPF texture maps of the (c) BCC and (d) FCC phases, obtained from the tensile-tested

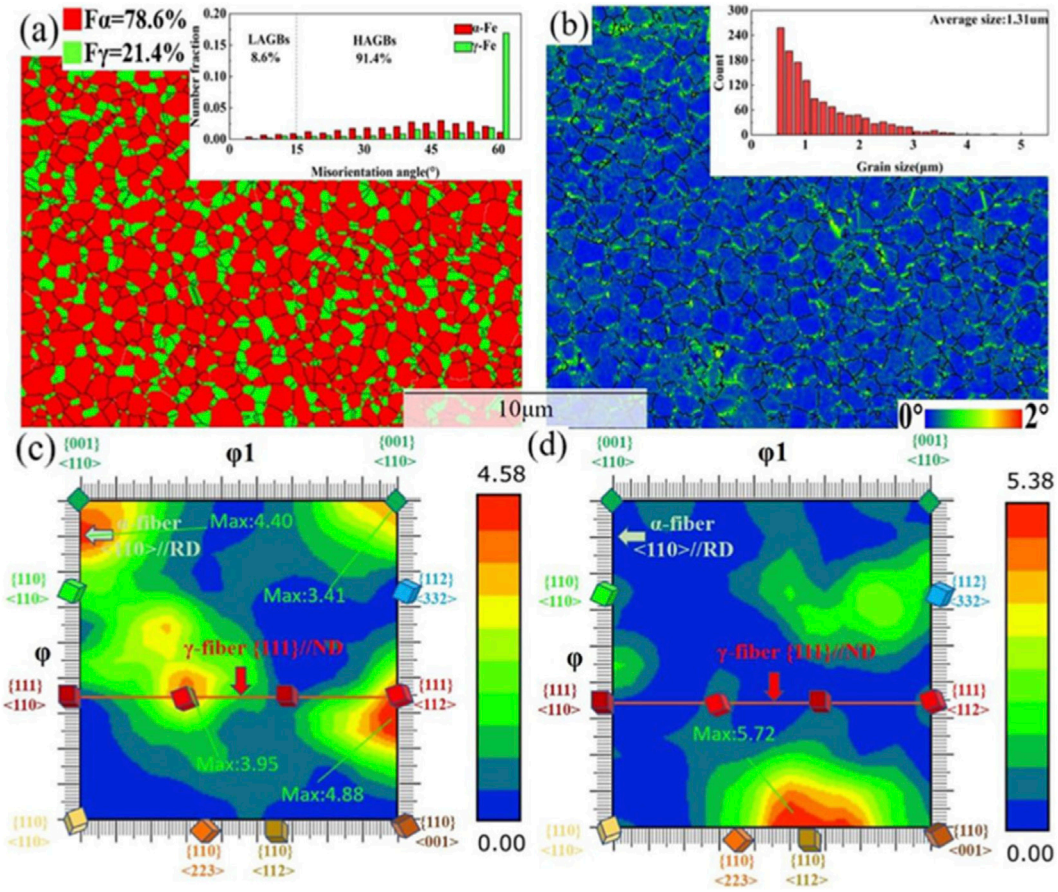

FIGURE 8
Microstructure of HTTT at 750 °C up to 0.9 true strain and strain rate of 1×10^{-3} s^{-1}: **(a)** Phase and grain boundaries map, **(b)** Kernel average misorientation map and grain size statistics image, **(c)** ODF of the BCC phase, and **(d)** ODF of the FCC phase. Adopted with permission (Pan et al., 2023a).

IA750 sample near the fracture surface. The BCC grains exhibit pronounced crack propagation and arrest along {111} orientations, reflected in the strong texture intensities. In contrast, the FCC phase shows smoother crack paths and a broader orientation distribution, consistent with enhanced slip and twinning activity. In the FCC phase, most RA grains are oriented along the ⟨101⟩ direction, while a smaller number are distributed between the ⟨101⟩ and ⟨111⟩ directions. The combined analysis highlights the distinct deformation and fracture responses of the two phases, underscoring their complementary roles in strength–ductility balance.

6 Overview of the review work

The rotation and orientation of grains following deformation significantly affect the mechanical properties of steel, as the crystallographic texture plays a crucial role in influencing mechanical anisotropy (Kumar et al., 2025b). In crystallography, the texture is represented as {HKL}. For rolled steel sheets, this notation indicates the orientation of crystal planes that align with the rolling plane (RP) and the rolling direction (RD). Key deformation textures include α-fibers, ε-fibers, and γ-fibers, which are associated with specific fiber axes along the RD, transverse direction (TD), and normal direction (ND), respectively (Nafisi et al., 2012). The {332} component is known for optimally balancing strength and toughness, while the {113} and {112} textures tend to increase mechanical anisotropy (Ray and Jonas, 1990). Observations indicate the development of {100}, {113}, and {332} textures across different thermomechanical processing routes, with the {332} and {113} components arising from orientations found in deformed austenite (Venkatsurya et al., 2013). It was noticed that the primary deformation textures in X70 and X80 pipeline steels are the α-fiber (//RD), γ-fiber (//ND), and ε-fiber (//TD). The {112}, {113}, and {223} components contribute to the anisotropy in YS (Venkatsurya et al., 2012). The orientation of neighboring grains plays a significant role in crack propagation (Baczynski et al., 1999). Specifically, {001} planes increase the risk of brittle fracture, while grains with a {001}//normal plane (NP) orientation decrease transgranular and intergranular low-resistance paths (Wright and Field, 1998). This reduction leads to crack coalescence and stepwise hydrogen-induced cracking. Conversely, {111}//NP textures foster high-resistance intergranular crack paths. Furthermore, {001} planes act as primary pathways for transgranular cleavage, which can result in sudden brittle failure

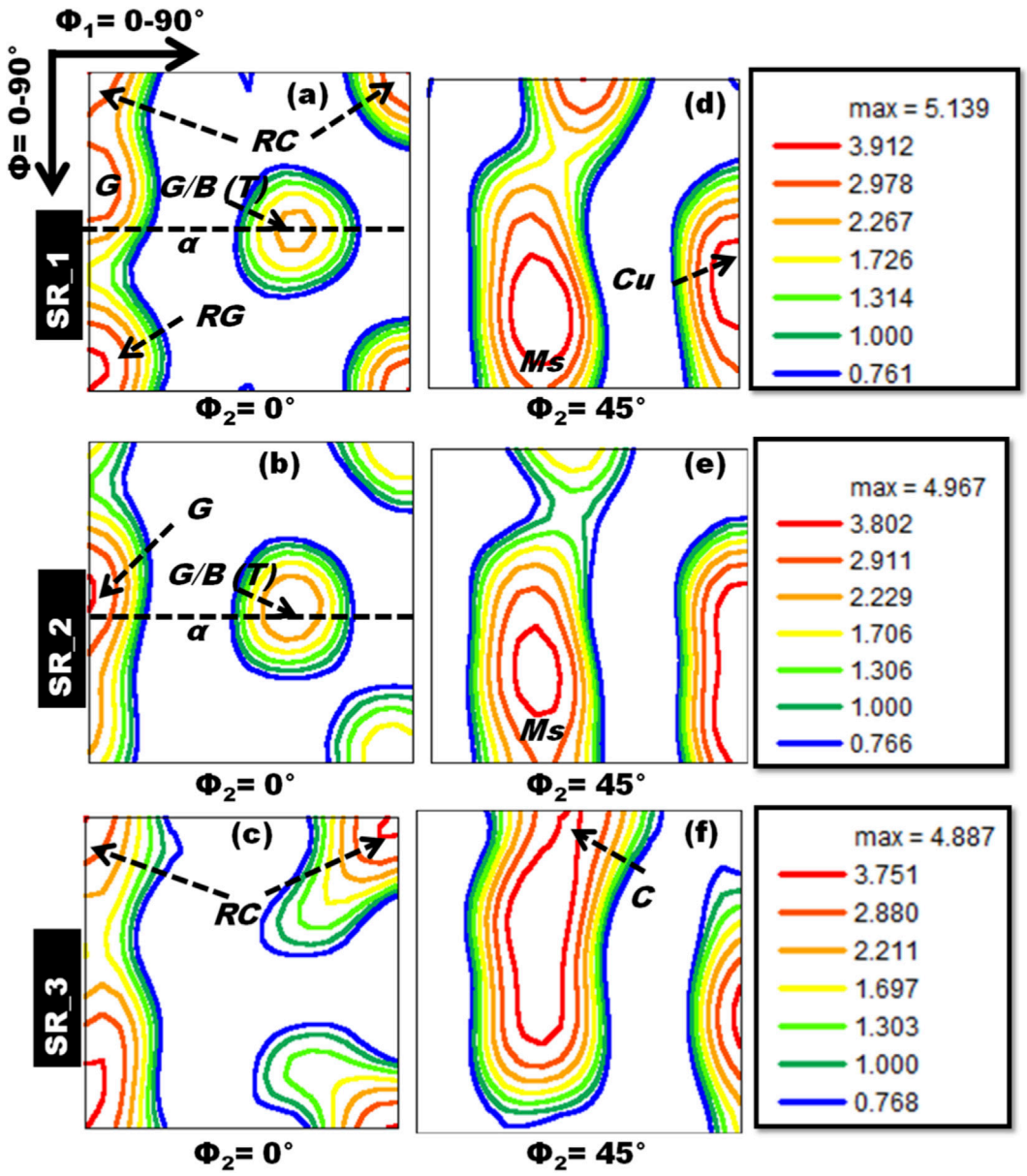

FIGURE 9
ODF sections of FCC-austenite in the tensile-strained samples at φ_2 = 0° **(a,b,c)** and 45° **(d,e,f) (a,d)** SR_1, **(b,e)** SR_2, and **(c,f)** SR_ 3. Important textural components are shown. RC, rotated cube {001} ⟨110⟩; C, cube {100} ⟨001⟩; Ms, MS brass {011} ⟨211⟩; α-fiber {011}//ND; Cu, copper {112} ⟨111⟩; G, Goss {011} ⟨100⟩; G/B (T), Goss/brass twin {011} ⟨111⟩; RG, rotated Goss component {011} ⟨011⟩. Adopted with permission (Mohapatra et al., 2023f).

when aligned with the fracture surface. It was found that emphasized that grains textured with the {111}//rolling plane can reduce crack propagation in steels (Razmpoosh et al., 2020). Numerous studies have examined the influence of thermo-mechanical control rolling parameters on crystallographic texture and microstructure, particularly drawing attention to the importance of finish rolling temperature in achieving deformation texture in low-alloy steel (Omale et al., 2017). Lower temperatures promote the {111} texture, whereas higher temperatures result in diminished intensity (Guo et al., 2008). Furthermore, the development of a cube ({100}) texture is linked to a decrease in the tensile properties of medium-Mn steel, as the {100} plane functions as a cleavage plane in BCC materials (Wang et al., 2022). Conversely, grains aligned in the {111} and {110} directions enhance ductility and tensile properties, leading to improved strength due to the formation of γ-fiber {111}//ND and brass {110} textures through thermo-mechanical processing (Pan et al., 2023a). However, the precise effect of these textures on crack susceptibility remains unclear. Texture evolution is critically important for determining mechanical properties, particularly the stability of austenite against martensitic transformation, which is influenced by the crystal orientation in relation to applied stress (Yan et al., 2018). During the martensitic transformation, the selection of variants impacts texture; however, mechanisms such as crystal rotation and twinning

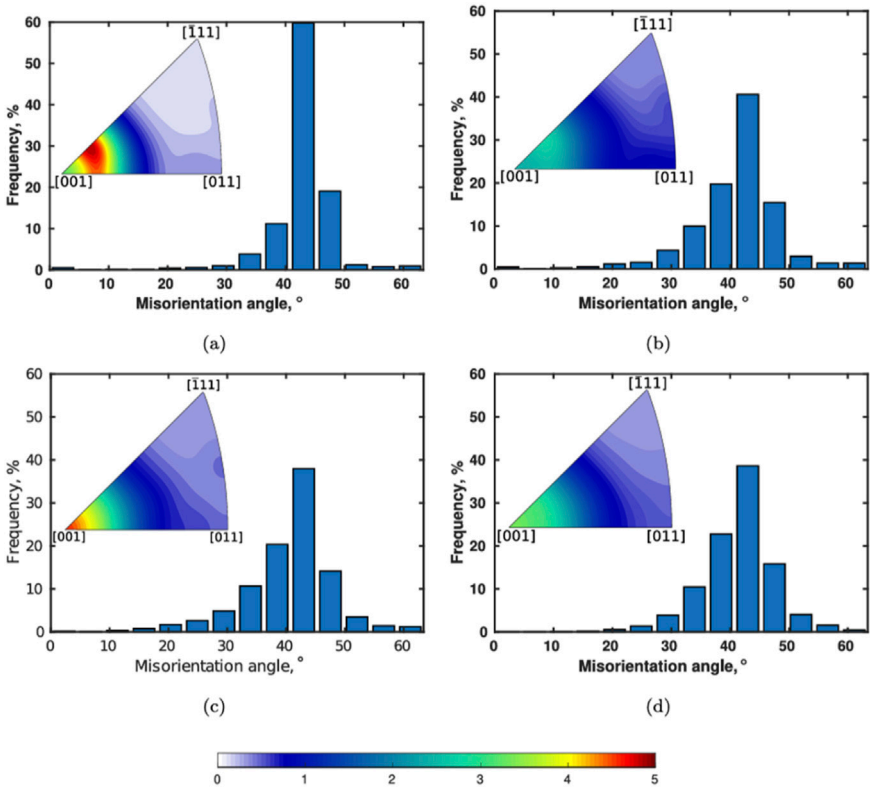

FIGURE 10
The misorientation angle and axis distribution of fcc/bcc boundaries for the samples deformed at **(a)** 10^{-3} s^{-1} (RT), **(b)** 1 s^{-1} (RT), **(c)** 103 s^{-1} (RT), and **(d)** 10^{-3} s^{-1} (409 K) to the true plastic strain of ~0.25. Adopted with permission (Patra et al., 2024).

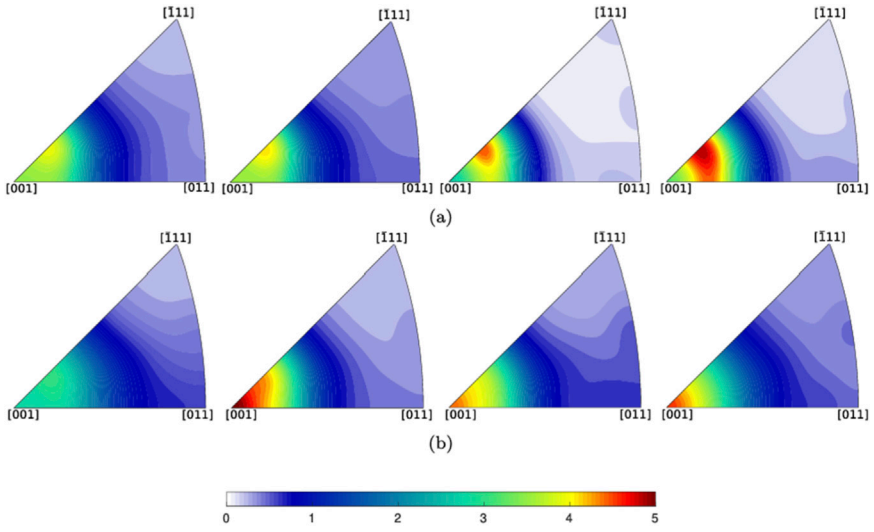

FIGURE 11
The misorientation axis distribution of fcc/bcc boundaries for the samples deformed at **(a)** 10^{-3} s^{-1} (RT) and **(b)** 10^{3} s^{-1} (RT) to the intermediate strains of around 0.1, 0.15, 0.2, and 0.25, respectively (from left to right). Adopted with permission (Patra et al., 2024).

also contribute significantly (Wang et al., 2014). Recent studies suggest that the rotation of austenite during deformation improves the ductility of traditional TRIP steels by serving as a barrier to dislocation movement, thereby delaying the onset of crack formation (Tirumalasetty et al., 2012). Observations made during tensile testing reveal increased intensity in certain orientations of austenite and martensitic structures, indicating a stress-assisted transformation (Morales-Rivas et al., 2018). This suggests that

10.3389/fmats.2026.1954859

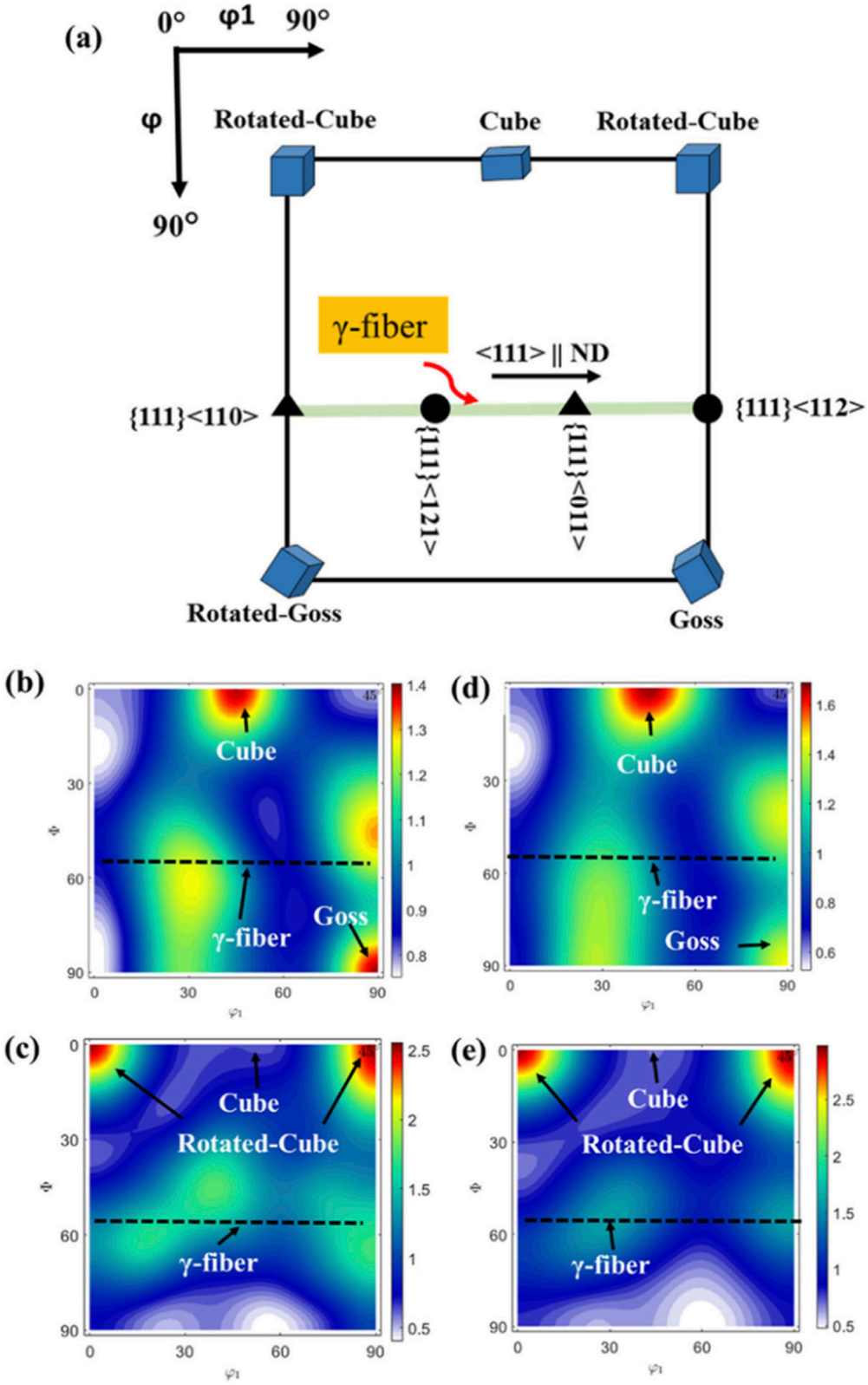

FIGURE 12
(a) The standard ODF section at φ_2 = 45° with important components of BCC material. The **(b,c)** experimental and **(d,e)** simulated micro-textures of **(b,d)** HF and **(c,e)** HR specimens are also shown. Adopted with permission (Kumar et al., 2023).

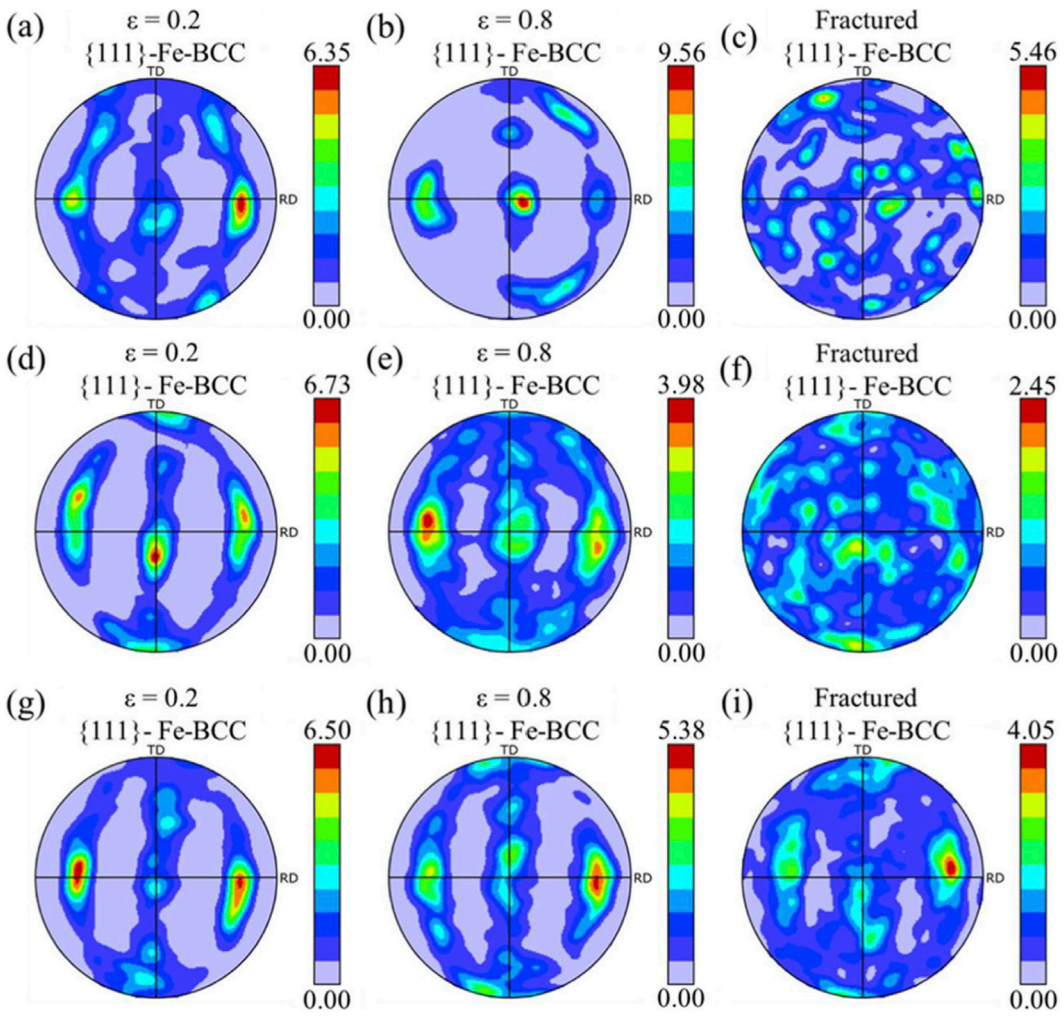

FIGURE 13
Pole figures of the BCC phase for the HTT samples at different deformation stages: **(a, d, g)** 5×10^{-4} s^{-1}, **(b, e, h)** 5×10^{-3} s^{-1}, **(c, f, i)** 2.5×10^{-2} s^{-1}. Adopted with permission (Pan et al., 2023c).

both stress and the accommodation of martensite twins play vital roles in texture development, extending beyond mere interactions between stress direction and shape change strain. Comparative overview of ferritic, austenitic, and duplex medium-Mn steels, highlighting Mn range, dominant phases, texture components, operative mechanisms, and their mechanical implications is shown in Table 8. In addition, Table 9 shows the influence of key alloying elements (Mn, Ni, C, Al, Si) on phase stability, stacking fault energy, austenite reversion, and texture development in medium-Mn steels.

7 Research gaps, challenges, and perspectives

The research on MMnSs faces several unresolved challenges that intersect various domains. Current predictive models are unable to accurately represent the complex interplay between TRIP and TWIP under industrial conditions. Additionally, dynamic processes such as austenite reversion and twinning have not been thoroughly explored due to limited *in situ* characterization techniques. Findings related to texture control from laboratory experiments require further validation through pilot-scale trials to ensure that they can be scaled effectively for industrial applications. The understanding of corrosion-mechanical coupling is notably inadequate, with a particular lack of insight into how grain boundary character distribution affects long-term performance of the steels. Moreover, welding and joining processes often lead to the degradation of the γ fiber in heat-affected zones, which compromises the mechanical integrity of the materials. Furthermore, alloy design is hindered by a lack of systematic frameworks for optimizing combinations of manganese, nickel, carbon, aluminum, and silicon, while the fatigue performance of these steels under cyclic loading conditions has not been sufficiently researched. Collectively, these gaps underscore the pressing need for integrated modeling approaches, advanced real-time characterization methods, scalable processing strategies, and comprehensive evaluations of service performance to advance

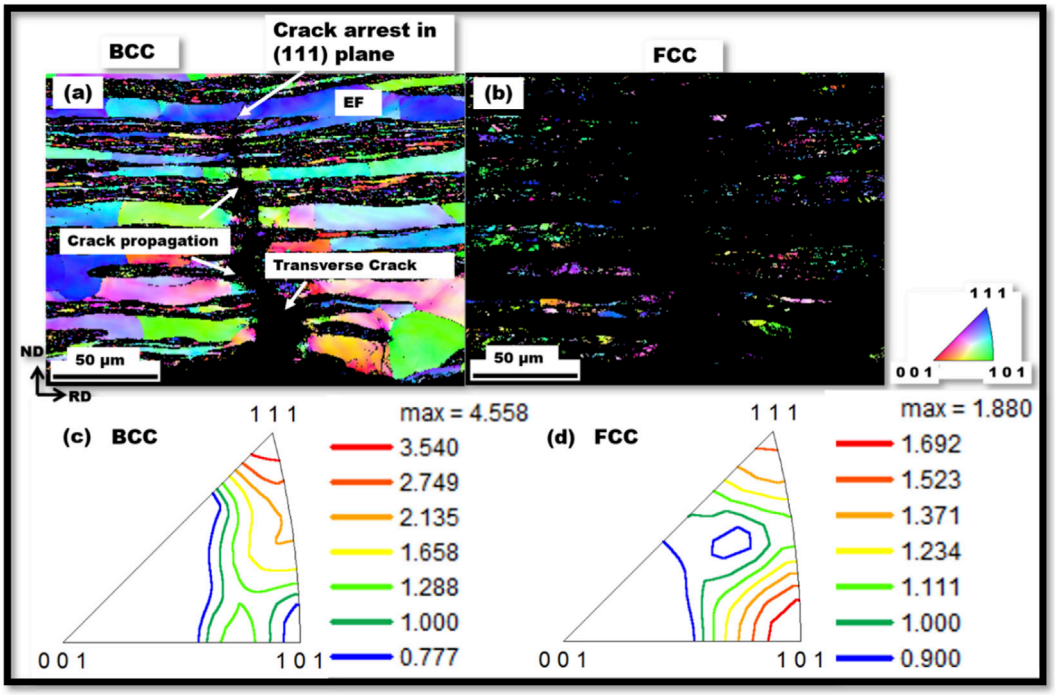

FIGURE 14
IPF maps of the **(a)** BCC and **(b)** FCC phases, and the IPF texture maps of the **(c)** BCC and **(d)** FCC phases of the tensile-tested IA750 sample near the fracture surface. Adopted with permission (Mohapatra et al., 2024d).

TABLE 8 **Classification of medium-Mn steels (ferritic, austenitic, duplex) with Mn range, dominant phases, texture components, operative mechanisms, and mechanical implications.**

MMnS Class	Mn range	Dominant phases	Texture components	Mechanisms	Mechanical implications
Ferritic	3–6 wt%	α-ferrite + minor γ	Cube, α-fiber, weak γ-fiber	Slip, limited TRIP	High strength, limited ductility
Austenitic	9–12 wt%	γ-austenite	Strong γ-fiber, {111}, {110}	TWIP, slip	Exceptional ductility, moderate strength
Duplex	6–9 wt%	Ferrite + γ-austenite	Cube, α-fiber, strong γ-fiber	TRIP + TWIP synergy	Optimal strength–ductility balance

TABLE 9 **Comparative summary of the influence of alloying elements.**

Element	Phase stability	SFE effect	Austenite reversion	Texture contribution
Mn	γ-stabilization	↑ SFE	Accelerates reversion	Strengthens γ-fiber
Ni	γ- stabilization	↑ SFE	Stabilizes reverted γ	Strengthens γ-fiber
C	γ stabilization	↑ SFE	Accelerates reversion	Strengthens γ-fiber
Al	Ferrite stabilization	↓ SFE	Retards reversion	Promotes cube, twinning reorientation
Si	Suppresses carbides	↓ SFE	Aids reversion	Facilitates twinning, strengthens {111}

the field of MMnSs. Future research must integrate advanced characterization and predictive modeling to bridge laboratory findings with industrial processing, ensuring MMnSs fulfill their potential as next-generation automotive steels.

8 Conclusion

This review highlights that texture development in medium-Mn steels is intrinsically linked to their phase constitution, alloying

chemistry, and thermomechanical processing. The following are the conclusions derived from the current review of texture development in medium manganese steel.

I. Medium-Mn steels are advanced high-strength steels characterized by the interaction of phase constitution, texture evolution, and deformation mechanisms. Ferritic grades, primarily composed of α-ferrite, offer high yield strength and stability but have limited ductility, relying on the TRIP effect. Austenitic grades, with increased Mn and Ni, provide outstanding ductility through the TWIP effect, though they sacrifice some strength and increase costs. Duplex steels, which balance ferrite and austenite, combine TRIP and TWIP effects, resulting in beneficial strength-ductility combinations and mechanical isotropy.
II. The roles of alloying elements are crucial: Mn stabilizes γ-fiber and supports the TRIP/TWIP mechanisms; Ni improves grain refinement and slip/twinning; carbon (C) stabilizes retained austenite and influences texture; aluminum (Al) suppresses carbide formation and promotes cube textures in ferrite; while silicon (Si) enhances austenite stability and reduces anisotropy. Precise control over these elements is essential, as imbalances can adversely affect toughness, corrosion resistance, and texture consistency.
III. Processing conditions, including intercritical annealing temperatures, cold rolling, and thermomechanical treatments, significantly influence the texture evolution and mechanical behavior of the steels. The transitions among various orientations (cube, α-fiber, brass, γ-fiber) illustrate the sensitivity of Medium-Mn steels to strain paths and thermal histories, highlighting the necessity for predictive models that incorporate alloy composition, phase transformation kinetics, and texture development.
IV. Ultimately, Medium-Mn steels provide a customizable framework for achieving optimal strength-ductility relationships through deliberate microstructural design and texture engineering. They are particularly valuable for automotive and structural applications, where safety and formability are critical. Future research should focus on integrated alloy design, advanced characterization techniques, and process optimization to fully exploit the capabilities of Medium-Mn steels while addressing challenges related to cost, segregation, and corrosion resistance.

Author contributions

SM: Conceptualization, Data curation, Formal Analysis, Investigation, Methodology, Supervision, Writing – original draft, Writing – review and editing. RP: Formal Analysis, Writing – review and editing. BM: Formal Analysis, Writing – review and editing. PS: Writing – review and editing.

Funding

The author(s) declared that financial support was received for this work and/or its publication. Authors thank the OUTR, Bhubaneswar, for the support.

Conflict of interest

The author(s) declared that this work was conducted in the absence of any commercial or financial relationships that could be construed as a potential conflict of interest.

Generative AI statement

The author(s) declared that generative AI was not used in the creation of this manuscript.

Any alternative text (alt text) provided alongside figures in this article has been generated by Frontiers with the support of artificial intelligence and reasonable efforts have been made to ensure accuracy, including review by the authors wherever possible. If you identify any issues, please contact us.

Publisher's note

All claims expressed in this article are solely those of the authors and do not necessarily represent those of their affiliated organizations, or those of the publisher, the editors and the reviewers. Any product that may be evaluated in this article, or claim that may be made by its manufacturer, is not guaranteed or endorsed by the publisher.

References

Alam, M. I., Wipp, S., Chandan, A. K., Mishra, G., Shekhar, S., Bleck, W., et al. (2026). Strain rate dependent deformation behavior evolution and ensuing tensile properties of a medium manganese steel. *Mater. Sci. Eng. A* 972, 150587. doi: 10.1016/j.msea.2026.150587

Aliabad, R. S., Sadeghpour, S., Karjalainen, P., Kömi, J., Singh, H., and Javaheri, V. (2025). Carbon redistribution in a martensitic medium Mn steel during heating to intercritical region: an *in-situ* synchrotron XRD study. *Procedia Struct. Integr.* 69:69–75. doi: 10.1016/j.prostr.2025.07.010

Baczynski, G. J., Jonas, J. J., and Collins, L. E. (1999). The influence of rolling practice on notch toughness and texture development in high-strength linepipe. *Metall. Mater. Trans. A* 30, 3045–3054. doi: 10.1007/s11661-999-0215-5

Bai, S., Xiao, W., Niu, W., and Liang, W. (2021). Microstructure and mechanical properties of a medium-mn steel with 1.3 gpa-strength and 40%-ductility. *Mater. (Basel)* 14, 2233. doi: 10.3390/ma14092233

Barbier, D., Gey, N., Allain, S., Bozzolo, N., and Humbert, M. (2009). Analysis of the tensile behavior of a TWIP steel based on the texture and microstructure evolutions. *Mater. Sci. Eng. A* 500, 196–206. doi: 10.1016/j.msea.2008.09.031

Bhadeshia, HKDH (2005). High performance bainitic steels. *Mater. Sci. Forum* 500–501, 63–74. doi: 10.4028/0-87849-981-4.63

Cai, M., Li, Z., Chao, Q., and Hodgson, P. D. (2014). A novel Mo and Nb microalloyed medium Mn TRIP steel with maximal ultimate strength and moderate ductility. *Metall. Mater. Trans. A Phys. Metall. Mater. Sci.* 45, 5624–5634. doi: 10.1007/s11661-014-2504-x

Cai, Z. H., Cai, B., Ding, H., Chen, Y., and Misra, R. (2016). Microstructure and deformation behavior of the hot-rolled medium manganese steels with varying aluminum-content. *Mater. Sci. Eng. A* 676, 263–270. doi: 10.1016/j.msea.2016.08.119

Cai, Z. H., Jing, S. Y., Li, H. Y., Zhang, K., Misra, R., Ding, H., et al. (2019). The influence of microstructural characteristics on yield point elongation phenomenon in Fe-0.2C-11Mn-2Al steel. *Mater. Sci. Eng. A* 739, 17–25. doi: 10.1016/j.msea.2018.09.114

Capek, J., Cernik, M., Ganev, N., Trojan, K., Nemecek, J., and Kolarik, K. (2018). Comparison of rolling texture of austenite and ferrite phases of duplex steel with single-phase austenitic and ferritic steel. *IOP Conf. Ser. Mater. Sci. Eng.* 375, 012025. doi: 10.1088/1757-899X/375/1/012025

Cen, Q., Wang, W., Zhang, B., Yan, Z., Wang, Y., and Zhang, M. (2022). Influence of Ni addition on the microstructure and mechanical properties of 3.5Mn Medium-Mn steel. *Metall. Mater, Trans. A Phys. Metall. Mater, Sci.* 53, 4034–4046. doi: 10.1007/s11661-022-06808-w

Chen, S., Rana, R., Haldar, A., and Ray, R. K. (2017). Current state of Fe-Mn-Al-C low density steels. *Prog. Mater. Sci.* 89, 345–391. doi: 10.1016/j.pmatsci.2017.05.002

Cheng, P., Hu, B., Liu, S. L., Guo, H., Enomoto, M., and Shang, C. (2019). Influence of retained austenite and Cu precipitates on the mechanical properties of a cold-rolled and intercritically annealed medium Mn steel. *Mater, Sci. Eng. A* 746, 41–49. doi: 10.1016/j.msea.2018.12.111

Choi, H., Lee, S., Lee, J., Barlat, F., and De Cooman, B. C. (2017). Characterization of fracture in medium Mn steel. *Mater, Sci. Eng. A* 687, 200–210. doi: 10.1016/j.msea.2017.01.055

Dai, Z., Ding, R., Yang, Z., Zhang, C., and Chen, H. (2018). Thermo-kinetic design of retained austenite in advanced high strength steels. *Acta Mater,* 152, 288–299. doi: 10.1016/j.actamat.2018.04.040

Dalai, R., Mohapatra, S., Das, S., and Das, K. (2023). Effect of thermo – processing on the microstructure, impact abrasion wear, and corrosion resistance properties of TiC reinforced Al-Added High-Mn steel matrix composite. *JOM* 75, 5281–5289. doi: 10.1007/s11837-023-05974-5

Dalai, R. P., Mohapatra, S., Padhy, A., and Pradhan, R. (2026). Influence of annealing temperature on the microstructure and tensile properties of hot-rolled high-C, high-Mn steel. *Mater. Lett.* 424:141525. doi: 10.1016/j.matlet.2026.141525

De Cooman, B. C., Kwon, O., and Chin, K. G. (2012). State-of-the-knowledge on TWIP steel. *Mater. Sci. Technol.* 28, 513–527. doi: 10.1179/1743284711Y.0000000095

Dutta, A., Ponge, D., Sandlöbes, S., and Raabe, D. (2019). Strain partitioning and strain localization in medium manganese steels measured by *in situ* microscopic digital image correlation. *Materialia* 5, 100252. doi: 10.1016/j.mtla.2019.100252

Ghosh, A., Kundu, S., and Chakrabarti, D. (2014). Effect of crystallographic texture on the cleavage fracture mechanism and effective grain size of ferritic steel. *Scr Mater.* 81, 8–11. doi: 10.1016/j.scriptamat.2014.02.007

Ghosh, A., Patra, S., Chatterjee, A., and Chakrabarti, D. (2016). Effect of local crystallographic texture on the fissure formation during charpy impact testing of low-carbon steel. *Metall. Mater. Trans. A Phys. Metall. Mater. Sci.* 47, 2755–2772. doi: 10.1007/s11661-016-3458-y

Grajcar, A., Kilarski, A., and Kozlowska, A. (2018). Microstructure–property relationships in thermomechanically processed medium-Mn steels with high Al content. *Met. (Basel)* 8, 1–19. doi: 10.3390/met8110929

Guo, Y., Wang, Z., Zou, W., Liu, X. h., and Wang, G. d. (2008). Textures and properties of hot rolled high strength Ti-IF steels. *J. Iron Steel Res. Int.* 15, 70–76. doi: 10.1016/S1006-706X(08)60252-6

Han, Y., Shi, J., Xu, L., Cao, W., and Dong, H. (2011). TiC precipitation induced effect on microstructure and mechanical properties in low carbon medium manganese steel. *Mater. Sci. Eng. A* 530, 643–651. doi: 10.1016/j.msea.2011.10.037

Han, J., da Silva, A. K., Ponge, D., Raabe, D., Lee, S. M., Lee, Y. K., et al. (2017). The effects of prior austenite grain boundaries and microstructural morphology on the impact toughness of intercritically annealed medium Mn steel. *Acta Mater.* 122:199–206. doi: 10.1016/j.actamat.2016.09.048

Hu, B., Luo, H., Yang, F., and Dong, H. (2017). Recent progress in medium-Mn steels made with new designing strategies, a review. *J. Mater. Sci. Technol.* 33, 1457–1464. doi: 10.1016/j.jmst.2017.06.017

Hu, B., He, B. B., Cheng, G. J., Yen, H., Huang, M., and Luo, H. (2019). Super-high-strength and formable medium Mn steel manufactured by warm rolling process. *Acta Mater.* 174, 131–141. doi: 10.1016/j.actamat.2019.05.043

Hu, C., Huang, C. P., Liu, Y. X., Perlade, A., Zhu, K., and Huang, M. (2023). The dual role of TRIP effect on ductility and toughness of a medium Mn steel. *Acta Mater.* 245, 118629. doi: 10.1016/j.actamat.2022.118629

Hui, W., Shao, C., Zhang, Y., Zhao, X., and Weng, Y. (2017). Microstructure and mechanical properties of medium Mn steel containing 3%Al processed by warm rolling. *Mater. Sci. Eng. A* 707, 501–510. doi: 10.1016/j.msea.2017.09.090

Hutchinson, B., Ryde, L., and Bate, P. (2005). Transformation-textures in steels. *Mater. Sci. Forum* 495–497, 1141–1150. doi: 10.4028/0-87849-975-x.1141

Jacob, R., Raman Sankaranarayanan, S., and Kumaresh Babu, S. P. (2019). "Recent advancements in manganese steels-A review," in *Materials Today: Proceedings* (Elsevier Ltd), 2852–2858.

Jia, N. N., Guo, K., He, Y. M., Wang, Y., Peng, J., and Wang, T. (2017). A thermomechanical process to achieve mechanical properties comparable to those of quenched-tempered medium-C steel. *Mater. Sci. Eng. A* 700, 175–182. doi: 10.1016/j.msea.2017.06.011

Kishore, K., Chandan, A. K., Purty, M., Karthik, V., Mishra, G., Kumar Sahoo, B., et al. (2023). Effect of microstructure on corrosion behavior of medium manganese steel. *Mater Lett.* 330, 133344. doi: 10.1016/j.matlet.2022.133344

Kumar, S., Rakshit, R., Prasad, A. D., Jayabalan, B., Mukherjee, S., and Mandal, S. (2023). Excellent strength-ductility synergy in a novel medium manganese steel containing 2.4Al-2.9Mn-4.1Ni realized through limited thermo-mechanical processing steps. *Mater, Sci. Eng. A* 883, 145488. doi: 10.1016/j.msea.2023.145488

Kumar, S., Ghosh, D., Rakshit, R., Mukherjee, S., and Mandal, S. (2025a). Unveiling the correlation among microstructure, texture, slip system activity, and tensile property in a hot rolled Ni containing Medium Mn steel. *Steel Res. Int.* 96:2400537. doi: 10.1002/srin.20400537

Kumar, S., Ghosh, D., Rakshit, R., Mukherjee, S., and Mandal, S. (2025b). Unveiling the correlation among microstructure, texture, slip system activity, and tensile property in a hot rolled Ni containing Medium-Mn steel. *Steel Res. Int.* 96, 2400537. doi: 10.1002/srin.202400537

Kwok, T. W. J., Worsnop, F. F., Douglas, J. O., and Dye, D. (2023). Carbon in solution and the charpy impact performance of medium Mn steels. *Metall. Mater, Trans. A* 54, 4128–4137. doi: 10.1007/s11661-023-07157-y

Lamari, M., Geandier, G., Nakonechna, O., Perlade, A., Zhu, K., and Allain, S. (2026). *In situ* quantification of cementite precipitation/dissolution kinetics and austenite carbon enrichment in medium Mn steels. *Mater, Des.* 265:115966. doi: 10.1016/j.matdes.2026.115966

Lee, Y. K., and Han, J. (2015). Current opinion in medium manganese steel. *Mater, Sci. Technol. (United Kingdom)* 31, 843–856. doi: 10.1179/1743284714Y.0000000722

Lee, S., Estrin, Y., and De Cooman, B. C. (2013). Constitutive modeling of the mechanical properties of V-added medium manganese TRIP steel. *Metall. Mater, Trans. A Phys. Metall. Mater. Sci.* 44, 3136–3146. doi: 10.1007/s11661-013-1648-4

Lee, H., Jo, M. C., Sohn, S. S., Zargaran, A., Ryu, J. H., Kim, N. J., et al. (2018). Novel medium-Mn (austenite + martensite) duplex hot-rolled steel achieving 1.6 GPa strength with 20 % ductility by mn-segregation-induced TRIP mechanism. *Acta Mater* 147, 247–260. doi: 10.1016/j.actamat.2018.01.033

Li, Z. C., Misra, R. D. K., Cai, Z. H., Li, H., and Ding, H. (2016). Mechanical properties and deformation behavior in hot-rolled 0.2C-1.5/3Al-8.5Mn-Fe TRIP steel: the discontinuous TRIP effect. *Mater. Sci. Eng. A* 673, 63–72. doi: 10.1016/j.msea.2016.07.023

Li, Z. C., Ding, H., Misra, R. D. K., and Cai, Z. H. (2017a). Microstructure-mechanical property relationship and austenite stability in medium-Mn TRIP steels: the effect of austenite-reverted transformation and quenching-tempering treatments. *Mater. Sci. Eng. A* 682, 211–219. doi: 10.1016/j.msea.2016.11.048

Li, Y., Li, W., Min, N., Liu, W., and Jin, X. (2017b). Effects of hot/cold deformation on the microstructures and mechanical properties of ultra-low carbon medium manganese quenching-partitioning-tempering steels. *Acta Mater.* 139, 96–108. doi: 10.1016/j.actamat.2017.08.003

Li, X., Song, R., Zhou, N., and Li, J. (2018a). Microstructure and tensile behavior of Fe-8Mn-6Al-0.2C low density steel. *Mater. Sci. Eng. A* 709, 97–104. doi: 10.1016/j.msea.2017.10.039

Li, X., Song, R., Zhou, N., and Li, J. (2018b). An ultrahigh strength and enhanced ductility cold-rolled medium-Mn steel treated by intercritical annealing. *Scr Mater.* 154, 30–33. doi: 10.1016/j.scriptamat.2018.05.016

Li, Q., Sun, Y., Zuo, H., Feng, J., Li, Z., Cai, Z., et al. (2024). Microstructure evolution and mechanical properties of light medium manganese steel: different rolling directions during warm stamping. *J. Mater. Eng. Perform.* 33, 13882–13896. doi: 10.1007/s11665-023-08998-9

Lin, Z., Zhou, W., Hu, C., Zhang, S. l., Hu, F., Xu, K., et al. (2026). Effect and mechanism of Al content on the microstructure and low-temperature impact toughness of warm-rolled and tempered medium-Mn steels. *J. Mater. Res. Technol.* 43:3590–3602. doi: 10.1016/j.jmrt.2026.06.303

Liu, L., He, B., and Huang, M. (2018). The role of transformation-induced plasticity in the development of advanced high strength steels. *Adv. Eng. Mater.* 20, 1701083. doi: 10.1002/adem.201701083

Liu, S., Zhang, M., Liu, Z., Jin, M., Chen, L., Cai, X., et al. (2025). The study of austenite reverse transformation and grain refinement mechanisms in medium manganese steel during intercritical annealing process. *Mater. Charact.* 227, 115345. doi: 10.1016/j.matchar.2025.115345

Luo, L., Li, W., Wang, L., Zhou, S., and Jin, X. (2017). Tensile behaviors and deformation mechanism of a medium Mn-TRIP steel at different temperatures. *Mater. Sci. Eng. A* 682, 698–703. doi: 10.1016/j.msea.2016.11.017

Ma, Y., Sun, B., Schökel, A., Song, W., Ponge, D., Raabe, D., et al. (2020). Phase boundary segregation-induced strengthening and discontinuous yielding in ultrafine-grained duplex medium-Mn steels. *Acta Mater.* 200, 389–403. doi: 10.1016/j.actamat.2020.09.007

Ma, C., Wang, J., Ma, Y., Jiao, F., Jia, Q., Zhang, L., et al. (2026). Silicon-dictated strain-hardening behavior and fracture resistance in 1300 MPa-grade medium Mn steels. *Mater. Charact.* 232, 116026. doi: 10.1016/j.matchar.2026.116026

Mandal, A. (2016). *Processing-Microstructure-Microtexture-Property Correlation of Duplex Stainless Steels*, 1–194.

Mao, P. N., Liu, J. J., Huang, X. M., Zhong, Z., Zhang, J., and Shi, Y. (2024). The effect of double intercritical annealing on micromechanical behavior of a medium Mn transformation induced plasticity steel investigated by *in situ* high energy X-ray diffraction. *Mater. Sci. Eng. A* 902, 146576. doi: 10.1016/j.msea.2024.146576

Mishra, G., Chandan, A. K., and Kundu, S. (2017). Hot rolled and cold rolled medium manganese steel: mechanical properties and microstructure. *Mater. Sci. Eng. A* 701, 319–327. doi: 10.1016/j.msea.2017.06.088

Mohapatra, S. K. (2023). *Development of Aluminum Added Medium Manganese Steel for Automotive Applications*.

Mohapatra, S., Das, K., and Das, S. (2022). Effect of annealing time on the microstructure and mechanical properties of aluminum added low-density medium manganese steel. *Mater. Lett.* 318, 132211. doi: 10.1016/j.matlet.2022.132211

Mohapatra, S., Kumar, S., Das, S., and Das, K. (2023a). Effect of strain rate on the microstructure evolution and tensile behavior of medium manganese steel. *Mater. Lett.* 330, 133243. doi: 10.1016/j.matlet.2022.133243

Mohapatra, S., Das, K., and Das, S. (2023b). Significance of intercritical annealing temperature on the impact behavior. *Mater. Lett.* 344, 134418. doi: 10.1016/j.matlet.2023.134418

Mohapatra, S., Poojari, G., Das, S., and Das, K. (2023c). Insights into the dynamic impact behavior of intercritically annealed automotive-grade Fe–7Mn–4Al –0.18C steel. *Mater. Sci. Eng. A* 887, 145769. doi: 10.1016/j.msea.2023.145769

Mohapatra, S., Palai, D., Satpathy, B., Das, S., and Das, K. (2023d). Electrochemical study of intercritically annealed Fe-0.18C-7Mn-4Al steel. *Mater. Today Commun.* 34, 105282. doi: 10.1016/j.mtcomm.2022.105282

Mohapatra, S., Mandal, A., Poojari, G., Das, S., and Das, K. (2023e). Influence of intercritical annealing temperature on microstructure, microtexture, and tensile behavior of TRIP-assisted medium manganese steel. *Materialia* 28, 101781. doi: 10.1016/j.mtla.2023.101781

Mohapatra, S., Das, K., and Das, S. (2023f). Study on strain distribution and texture evolution of Fe-0.18C-4Al-7Mn steel under different strain rate conditions. *Mater. Lett.* 354, 135343. doi: 10.1016/j.matlet.2023.135343

Mohapatra, S., Kumar Pradhan, S., and Oh, M.-S. (2024a). The impact of annealing temperature and time on the grain distribution and texture evolution of cold-rolled electric-furnace annealed low-carbon steel. *Mater. Lett.* 371, 136955. doi: 10.1016/j.matlet.2024.136955

Mohapatra, S., Poojari, G., Satpathy, B., Das, S., and Das, K. (2024b). A comprehensive study on the effect of annealing temperature on the tensile and impact behavior of automotive-grade medium manganese steel (Fe-6.22Mn-0.18C). *J. Mater. Eng. Perform.* 33, 5348–5363. doi: 10.1007/s11665-023-08861-x

Mohapatra, S., Baek, K. C., and Oh, M. S. (2024c). Intercritically annealed medium-manganese steel: insights into microstructural and microtextural evolution, strain distribution, and grain boundary characteristics. *Mater. (Basel)* 17, 2757. doi: 10.3390/ma17112757

Mohapatra, S., Mandal, A., Das, S., and Das, K. (2024d). Study on local strain distribution and grain boundary characteristics of tensile-deformed TRIP-assisted medium manganese steel. *Mater. Sci. Eng. A* 894, 146225. doi: 10.1016/j.msea.2024.146225

Mohapatra, S., Satpathy, B., Sarkar, A., Kumar, S., and Aich, S. (2025a). Recent advances in medium-manganese steel: a review of key findings, challenges, and future perspectives. *J. Mater. Sci.* 60, 9447–9528. doi: 10.1007/s10853-025-11010-5

Mohapatra, S., Kumar, A., Kumar, S., and Poojari, G. (2025b). Influence of strain rate on the tensile properties, misorientation distribution, and texture evolution of automotive-grade TRIP-Assisted advanced high-strength steel. *Mater. Lett.* 378, 137612. doi: 10.1016/j.matlet.2024.137612

Mohapatra, S., Sarkar, A., Kumar, S., Dalai, R., and Oh, M.-S. (2026a). Impact behavior of automotive grade medium manganese steel: reviews on current progress and challenges. *Mater. Sci. Technol.*

Mohapatra, S., Kumar, S., Arohi, A. C., Pradhan, R., and Mahapatra, B. N. (2026b). Influence of annealing time on microstructure and impact behavior of medium Mn-automotive steel. *Mater. Lett.* 418, 140832. doi: 10.1016/j.matlet.2026.140832

Mohapatra, S., Das, K., Das, S., and Satpathy, B. (2026c). Effect of annealing time on the static and accelerated corrosion behavior of medium manganese steel. *J. Mater. Sci.* 61, 32332–32356. doi: 10.1007/s10853-026-13739-z

Morales-Rivas, L., Archie, F., Zaefferer, S., Benito-Alfonso, M., Tsai, S. P., Yang, J. R., et al. (2018). Crystallographic examination of the interaction between texture evolution, mechanically induced martensitic transformation and twinning in nanostructured bainite. *J. Alloys Compd.* 752:505–519. doi: 10.1016/j.jallcom.2018.04.189

Nafisi, S., Arafin, M. A., Collins, L., and Szpunar, J. (2012). Texture and mechanical properties of API X100 steel manufactured under various thermomechanical cycles. *Mater. Sci. Eng. A* 531:2–11. doi: 10.1016/j.msea.2011.09.072

Omale, J. I., Ohaeri, E. G., Tiamiyu, A. A., Eskandari, M., Mostafijur, K., and Szpunar, J. (2017). Microstructure, texture evolution and mechanical properties of X70 pipeline steel after different thermomechanical treatments. *Mater. Sci. Eng. A* 703:477–485. doi: 10.1016/j.msea.2017.07.086

Pan, H., Chaofan, W., Zhang, H., Li, X., Liu, L., Li, J., et al. (2023a). Strain rate sensitivity of low-temperature superplastic cold-rolled medium Mn steel with ultrafine equiaxed dual-phase microstructure. *Mater. Sci. Eng. A* 873, 145025. doi: 10.1016/j.msea.2023.145025

Pan, H., Li, X., Zhang, H., Liu, L., Li, J., Zhao, Y., et al. (2023b). Achieving ultra-high elongation of 1401% in a warm-rolled medium Mn lightweight steel with dual-phase lamellar structure. *Mater. Sci. Eng. A* 862, 144493. doi: 10.1016/j.msea.2022.144493

Pan, H., Li, X., Zhang, S., Zhou, W., Wu, Z., and Liu, L. (2023c). Effect of strain rate on the microstructure evolution and superplastic deformation behavior of cold-rolled medium Mn lightweight steel. *Mater. Sci. Eng. A* 879, 145241. doi: 10.1016/j.msea.2023.145241

Patra, A. K., Kapoor, R., Mandal, S., K.C., H. K., and Vadlamani, S. S. (2024). Influence of strain rate on the work hardening, strain induced martensite formation, strain partitioning, and variant selection in a medium-Mn steel. *Mater. Sci. Eng. A* 902, 146593. doi: 10.1016/j.msea.2024.146593

Peng, F., Xu, Y., Gu, X., Wang, Y., Liu, X., and Li, J. (2018). The relationships of microstructure-mechanical properties in quenching and partitioning (Q&P) steel accompanied with microalloyed carbide precipitation. *Mater. Sci. Eng. A* 723, 247–258. doi: 10.1016/j.msea.2018.03.061

Pierce, D. T., Jiménez, J. A., Bentley, J., Raabe, D., and Wittig, J. (2015). The influence of stacking fault energy on the microstructural and strain-hardening evolution of Fe-Mn-Al-Si steels during tensile deformation. *Acta Mater.* 100, 178–190. doi: 10.1016/j.actamat.2015.08.030

Poojari, G., Kumar, H., Sampreeth, S., Tharian, T., Makineni, S. K., Singh, S. B., et al. (2024). Materialia effect of prior cold rolling and aging temperature on PH martensitic stainless steel: evolution of microstructure, micro-texture and austenite stability. *Materialia* 33, 102040. doi: 10.1016/j.mtla.2024.102040

Pradhan, R., Mohapatra, S., Sunny, M. R., and Sarkar, A. (2024). An investigation on microstructure-texture of E250BR steel plate subjected to post-weld vibration. *Proc. Inst. Mech. Eng. Part B J. Eng. Manuf.* 238, 514–523. doi: 10.1177/09544054231178972

Pütz, R. D., Allam, T., Wang, J., Nowak, J., Haase, C., Sandlöbes-Haut, S., et al. (2021). *Control of Electrochemical Corrosion Properties by Influencing Mn Partitioning Through Intercritically Annealing of Medium-Mn Steel*, 1–23.

Raabe, D. (1997). Texture and microstructure evolution during cold rolling of a strip cast and of a hot rolled austenitic stainless steel. *Acta Mater.* 45, 1137–1151. doi: 10.1016/S1359-6454(96)00222-4

Raabe, D., Ponge, D., Dmitrieva, O., and Sander, B. (2009). Nanoprecipitate-hardened 1.5 GPa steels with unexpected high ductility. *Scr Mater.* 60, 1141–1144. doi: 10.1016/j.scriptamat.2009.02.062

Ray, R. K., and Jonas, J. J. (1990). Transformation textures in steels. *Int. Mater. Rev.* 35, 1–36. doi: 10.1179/095066090790324046

Razmpoosh, M. H., Macwan, A., Biro, E., and Zhou, Y. (2020). Microstructure and dynamic tensile characteristics of dissimilar fiber laser welded advanced high strength steels. *Mater. Sci. Eng. A* 773, 138729. doi: 10.1016/j.msea.2019.138729

Ridlo, F., Zhang, B., Akkus, C., Gulbay, O., Chakraborty, A., Hu, B., et al. (2025). Influence of aluminum on microstructure and mechanical properties of air-hardened medium manganese steel. *Steel Res. Int.* 96, 2400869. doi: 10.1002/srin.202400869

Sahoo, B. K., Srivastava, V. C., Mahato, B., and Ghosh Chowdhury, S. (2021). Microstructure-mechanical property evaluation and deformation mechanism in Al added medium Mn steel processed through intercritical rolling and annealing. *Mater. Sci. Eng. A* 799, 140100. doi: 10.1016/j.msea.2020.140100

Sarkar, A., Sanyal, S., Bandyopadhyay, T. K., and Mandal, S. (2019). Implications of microstructure, Taylor factor distribution and texture on tensile properties in a Ti-added Fe-Mn-Al-Si-C steel. *Mater. Sci. Eng. A* 767, 138402. doi: 10.1016/j.msea.2019.138402

Seo, E. J., Cho, L., Estrin, Y., and De Cooman, B. C. (2016). Microstructure-mechanical properties relationships for quenching and partitioning (Q&P) processed steel. *Acta Mater.* 113, 124–139. doi: 10.1016/j.actamat.2016.04.048

Shao, C., Hui, W., Zhang, Y., Zhao, X., and Weng, Y. (2017). Microstructure and mechanical properties of hot-rolled medium-Mn steel containing 3% aluminum. *Mater. Sci. Eng. A* 682, 45–53. doi: 10.1016/j.msea.2016.11.036

Singh, A., Patra, A. K., Athreya, C. N., Sankaran, S., and Sarma, V. S. (2023). Role of Mn content on processing maps, deformation kinetics, microstructure and texture of as-cast medium Mn (6–10 wt% Mn) steels. *Mater. Sci. Eng. A* 884, 145500. doi: 10.1016/j.msea.2023.145500

Soleimani, M., Kalhor, A., and Mirzadeh, H. (2020). Transformation-induced plasticity (TRIP) in advanced steels: a review. *Mater. Sci. Eng. A* 795, 140023. doi: 10.1016/j.msea.2020.140023

Soliman, M., and Palkowski, H. (2014). Microstructure development and mechanical properties of medium carbon carbide-free bainite steels. *Procedia Eng.* 81, 1306–1311. doi: 10.1016/j.proeng.2014.10.148

Song, H., Kwon, Y., Sohn, S. S., Koo, M., Kim, N. J., Lee, B. J., et al. (2018). Improvement of tensile properties in (austenite+ferrite+κ-carbide) triplex hot-rolled lightweight steels. *Mater. Sci. Eng. A* 730, 177–186. doi: 10.1016/j.msea.2018.06.003

Sripushpa, K., Cheremisina, E., Inoue, R., Iwama, T., Ueda, S., and Kamaraj, A. (2026). Sustainable direct Mn alloying practice to produce medium Mn steel. *J. Sustain Metall.* 12, 1667–1680. doi: 10.1007/s40831-026-01420-3

Steineder, K., Krizan, D., Schneider, R., Béal, C., and Sommitsch, C. (2017). On the microstructural characteristics influencing the yielding behavior of ultra-fine grained medium-Mn steels. *Acta Mater.* 139, 39–50. doi: 10.1016/j.actamat.2017.07.056

Suh, D. W., and Kim, S. J. (2017). Medium Mn transformation-induced plasticity steels: recent progress and challenges. *Scr Mater.* 126, 63–67. doi: 10.1016/j.scriptamat.2016.07.013

Sun, B., Kwiatkowski da Silva, A., Wu, Y., Ma, Y., Chen, H., Scott, C., et al. (2022). Physical metallurgy of medium-Mn advanced high-strength steels. *Int. Mater. Rev.* 68, 786–824. doi: 10.1080/09506608.2022.2153220

Suwas, S., Ray, R. K., and Satyam Suwas, R. K. R. (2014). *Crystallographic Texture of Materials*.

Tirumalasetty, G. K., Van Huis, M. A., Kwakernaak, C., Sietsma, J., Sloof, W., and Zandbergen, H. (2012). Deformation-induced austenite grain rotation and transformation in TRIP-assisted steel. *Acta Mater.* 60, 1311–1321. doi: 10.1016/j.actamat.2011.11.026

Varanasi, R. S., Lipińska-Chwałek, M., Mayer, J., Gault, B., and Ponge, D. (2022). Mechanisms of austenite growth during intercritical annealing in medium manganese steels. *Scr Mater.* 206, 114228. doi: 10.1016/j.scriptamat.2021.114228

Venkatsurya, P. K. C., Jia, Z., Misra, R. D. K., Mulholland, M., Manohar, M., and Hartmann, J., Jr. (2012). Understanding mechanical property anisotropy in high strength niobium-microalloyed linepipe steels. *Mater. Sci. Eng. A* 556:194–210. doi: 10.1016/j.msea.2012.06.078

Venkatsurya, P. K. C., Misra, R. D. K., Mulholland, M. D., Manohar, M., and Hartmann, J., Jr. (2013). Effect of microstructure on the mechanical properties and texture in high strength 560MPa linepipe steels. *Mater. Sci. Eng. A* 575:6–14. doi: 10.1016/j.msea.2013.03.040

Wang, M. M., Tasan, C. C., Ponge, D., Kostka, A., and Raabe, D. (2014). Smaller is less stable: size effects on twinning vs. transformation of reverted austenite in TRIP-maraging steels. *Acta Mater.* 79, 268–281. doi: 10.1016/j.actamat.2014.07.020

Wang, X. G., Liu, C. H., He, B. B., Jiang, C., and Huang, M. (2019). Microscopic strain partitioning in Lüders band of an ultrafine-grained medium Mn steel. *Mater. Sci. Eng. A* 761, 138050. doi: 10.1016/j.msea.2019.138050

Wang, L., Zhou, P., Hu, Y., and Wang, B. (2022). Effect of microstructure and texture on the mechanical properties in high strength pipeline bend. *Int. J. Press Vessel Pip.* 195:104604. doi: 10.1016/j.ijpvp.2021.104604

Wang, M., Liang, X., Ren, W., Tong, S., and Sun, X. (2023). Effect of Mn content on the toughness and plasticity of hot-rolled high-carbon medium manganese steel. *Mater. (Basel)* 16, 2299. doi: 10.3390/ma16062299

Wright, S. I., and Field, D. P. (1998). Recent studies of local texture and its influence on failure. *Mater. Sci. Eng. A* 257:165–170. doi: 10.1016/S0921-5093(98)00835-1

Wu, Z., Jing, C., Feng, Y., Li, Z., Lin, T., Zhao, J., et al. (2023). Effect of a new pretreatment-Q&P process on the microstructure and mechanical properties of light-weight Al-containing medium-Mn steels. *Mater. Sci. Eng. A* 862, 144468. doi: 10.1016/j.msea.2022.144468

Xia, W., Zhao, X., Yue, L., and Zhang, Z. (2020). Microstructural evolution and creep mechanisms in Ni-based single crystal superalloys: a review. *J. Alloys Compd.* 819:152954. doi: 10.1016/j.jallcom.2019.152954

Xie, C., and Nakamachi, E. (2002). Investigations of the formability of BCC steel sheets by using crystalline plasticity finite element analysis. *Mater. Des. - MATER Des.* 23, 59–68. doi: 10.1016/S0261-3069(01)00043-7

Xu, L. L., Zheng, Z. B., Yang, H. K., Xu, Z. b., Long, J., Wang, S., et al. (2025). Adapting medium manganese steels for different wear conditions: insights from aluminum modification. *J. Iron Steel Res. Int.* 32, 3504–3519. doi: 10.1007/s42243-025-01516-2

Yadav, M. K., Kumar, D., Kumar, N., and Bandyopadhyay, T. K. (2023). Hot-rolled Al-added medium Mn steel (Fe-8Mn-2.85Al-1Si-0.2C): microstructural evolution and tensile behavior. *Materialia* 29, 101790. doi: 10.1016/j.mtla.2023.101790

Yan, S., Liu, X., Liang, T., and Zhao, Y. (2018). The effects of the initial microstructure on microstructural evolution, mechanical properties and reversed austenite stability of intercritically annealed Fe-6.1Mn-1.5Si-0.12C steel. *Mater. Sci. Eng. A* 712, 332–340. doi: 10.1016/j.msea.2017.11.118

Yan, S., Liang, T., Chen, J., Li, T., and Liu, X. (2019). A novel Cu-Ni added medium Mn steel: Precipitation of Cu-rich particles and austenite reversed transformation occurring simultaneously during ART annealing. *Mater. Sci. Eng. A* 746, 73–81. doi: 10.1016/j.msea.2019.01.014

Yang, Y. G., Mi, Z. L., Xu, M., Xiu, Q., Li, J., and Jiang, H. T. (2018). Impact of intercritical annealing temperature and strain state on mechanical stability of retained austenite in medium Mn steel. *Mater. Sci. Eng. A* 725, 389–397. doi: 10.1016/j.msea.2018.04.041

Yu, S., and Deng, Y. G. (2025). A review of recent developments in microstructures and mechanical properties of medium manganese steels. *J. Mater Eng. Perform.* 34, 16827–16846. doi: 10.1007/s11665-025-10669-w

Zhang, X., Miyamoto, G., Kaneshita, T., Yoshida, Y., Toji, Y., and Furuhara, T. (2018). Growth mode of austenite during reversion from martensite in Fe-2Mn-1.5Si-0.3C alloy: a transition in kinetics and morphology. *Acta Mater.* 154, 1–13. doi: 10.1016/j.actamat.2018.05.035

Zhang, B. G., Zhang, X. M., and Liu, H. T. (2020). Microstructural evolution and mechanical properties of Ni-containing light-weight medium-Mn TRIP steel processed by intercritical annealing. *Mater. Sci. Eng. A* 793, 139289. doi: 10.1016/j.msea.2020.139289

Zhang, X., Teng, R., Liu, T., Shi, Y., Lv, Z., Zhou, Q., et al. (2022). Improving strength–ductility synergy in medium Mn steel by combining heterogeneous structure and TRIP effect. *Mater. Charact.* 184, 111661. doi: 10.1016/j.matchar.2021.111661

Zhang, H. T., Li, H. Y., Yan, H. L., Tang, S., Beladi, H., Hodgson, P., et al. (2023). The effect of Ti-Mo additions on microstructural evolution and superplastic deformation behavior of cold–rolled medium Mn steels. *Mater. Charact.* 203, 113051. doi: 10.1016/j.matchar.2023.113051

Zhao, S., Song, R., Zhang, Y., Huo, W., Cai, C., Wang, Y., et al. (2023). Inhibition mechanism of heterogeneous grain structures on plastic instability behavior in 3Mn steel. *Mater. Sci. Eng. A* 874, 145083. doi: 10.1016/j.msea.2023.145083

Zhou, N., Song, R., Li, X., and Li, J. (2018). Dependence of austenite stability and deformation behavior on tempering time in an ultrahigh strength medium Mn TRIP steel. *Mater. Sci. Eng. A* 738, 153–162. doi: 10.1016/j.msea.2018.09.098

Zinsaz-borujerdi, A., Zarei-hanzaki, A., Abedi, H. R., Karam-Abian, M., Ding, H., Han, D., et al. (2018). Room temperature mechanical properties and microstructure of a low alloyed TRIP-assisted steel subjected to one-step and two-step quenching and partitioning process. *Mater. Sci. Eng. A* 725, 341–349. doi: 10.1016/j.msea.2018.04.042

Zou, Y., Xu, Y. B., Hu, Z. P., Chen, S., Han, D., Misra, R., et al. (2017). High strength-toughness combination of a low-carbon medium-manganese steel plate with laminated microstructure and retained austenite. *Mater. Sci. Eng. A* 707, 270–279. doi: 10.1016/j.msea.2017.09.059

Zuo, W., Yang, Y., Hu, Y., Li, R., Zhang, S., Wu, Y., et al. (2026). Role of initial microstructures in governing austenite reversion kinetics and morphology in medium manganese steel. *J. Mater. Res. Technol.* 40:1821–1837. doi: 10.1016/j.jmrt.2025.12.265